UNCLASSIFIED

AD __404 776__

DEFENSE DOCUMENTATION CENTER

FOR

SCIENTIFIC AND TECHNICAL INFORMATION

CAMERON STATION, ALEXANDRIA, VIRGINIA

UNCLASSIFIED

63-3-5

High-Dielectric-Constant Materials
and Ferroelectricity

by

A. von Hippel and co-workers

DDC

MAY 28 1963

TISIA A

404 776

AFCRL-63-92

High-Dielectric-Constant Materials and Ferroelectricity

by

A. von Hippel and co-workers

Laboratory for Insulation Research
Massachusetts Institute of Technology
Cambridge, Massachusetts

Final Report   March, 1963

·Prepared for

HIGH-DIELECTRIC-CONSTANT MATERIALS

AND FERROELECTRICITY

by

A. von Hippel

with the cooperation of

J. M. Ballantyne	R. Fuchs	T. Mitsui
V. Belruss	J. Hwang	C. W. Nelson
C. F. Buhrer	G. Jensen	S. Nomura
R. E. Charles	J. Kalnajs	M. J. Redman
T. R. Clevenger, Jr.	F. Kaczmarek	S. J. Waugh
V. Ern	E. Lewis	W. B. Westphal
E. F. Farrell	S. Lichtensteiger	A. Vetrovs
D. F. Fitzgerald	A. Linz	

Laboratory for Insulation Research
Massachusetts Institute of Technology
Cambridge, Massachusetts

ABSTRACT

This final report sums up the advances made during a tree year's study in: theoretical understanding of the onset and frequency response of ferroelectricity; techniques of growing single crystals and preparing ceramics of reproducible properties; chemical analysis and synthesis of high-dielectric-constant materials; effects of cation substitution; measurement techniques; and the interpretation of optical and electric spectra and conduction phenomena. The special subjects discussed in the theoretical Part I and the experimental Part II are enumerated in the Table of Contents.

PUBLICATIONS

Contract No. AF 19(604)-6155

Technical Reports

Tech. Rep. 160, Some Properties of Bismuth Perovskites, C. F. Buhrer, March, 1961.

Tech. Rep. 161, Behavior of Fe^{4+} in the System $SrFeO_3$-$SrTiO_3$, T. R. Clevenger, Jr., March, 1961.

Tech. Rep. 162, Dielectric and X-Ray Studies of $Ca_x Ba_{1-x} TiO_3$ and $Ca_x Sr_{1-x} TiO_3$, T. Mitsui and W. B. Westphal, March, 1961.

Tech. Rep. 163, Some Properties of Triglycine Sulfate, Guanidine Aluminum Sulfate Hexahydrate, and Triglycine Tellurate, F. Kaczmarek, June, 1961.

Tech. Rep. 164, Dipoles and Charge Carriers in Rutile, A. von Hippel, J. Kalnajs, and W. B. Westphal, June, 1961.

Tech. Rep. 167, Temperature Dependence of the Dielectric Constant of Ionic Crystals, R. Fuchs, November, 1961.

Publications

C. F. Buhrer, "Some Properties of Bismuth Perovskites," J. Chem. Phys. <u>36</u>, 798 (1962).

T. Mitsui and W. B. Westphal, "Dielectric and X-Ray Studies of $Ca_x Ba_{1-x} TiO_3$ and $Ca_x Sr_{1-x} TiO_3$," Phys. Rev. <u>124</u>, 1354 (1961).

A. von Hippel, J. Kalnajs, and W. B. Westphal, "Protons, Dipoles, and Charge Carriers in Rutile," J. Phys. Chem. Solids <u>23</u>, 779 (1962).

T. R. Clevenger, Jr., "Behavior of Fe^{4+} in the System $SrFeO_3$-$SrTiO_3$," J. Am. Ceram. Soc., in press.

Table of Contents

I. THEORETICAL DISCUSSION

Objectives and Approaches

High-dielectric-constant materials - at a first glance - seem the natural choice for concentrated electric-energy storage, but they have disappointed thus far. Ferroelectrics, similarly, should play a role in high-impedance devices commensurate to that of ferromagnetics in low-impedance ones, but again their importance as yet is inferior. The research here undertaken had the principal goal of contributing to the fundamental understanding of these classes of dielectrics and of helping to clarify their advantages and shortcomings.

It seems obvious that a research project of this kind calls for a three-step approach: preparation of materials, measurement of properties, interpretation of results. These steps, however, do not proceed in an orderly one-two-three sequence, because feedback effects continuously cause reappraisal and redirection. Methods of preparation have to be changed, until materials prove reproducible and their characteristics free of disturbing side effects. Observations remain obscure, until temperature and frequency ranges are extended and additional tools called in for physical and chemical analysis. Deepening insight leads to demands for better materials, new substitutions, additional data - and thus the research moves ahead until cut off at some arbitrary termination date.

As the Table of Contents indicates, new and improved materials have been made, fundamental insight has been gained, the inherent usefulness of the dielectrics at issue has become more clearly established. Simultaneously new problems have been raised, the work undertaken in this three-year study remains unfinished and will continue under other contracts.

Selection of Materials

A discussion of electric polarization phenomena usually starts with the polarization P, the dipole moment per unit volume, defined as

$$P = N\alpha E' \left[coul\ m^{-2} \right], \tag{1}$$

where

$$N\alpha = \frac{\alpha}{v} \left[\frac{coul^2\ sec^2}{kg\ m^3} \right] \tag{2}$$

designates the polarizability per unit volume, visualized as stemming from the additive action of N dipole carriers or volume elements with volume v. These dipole carriers or volume elements acquire an oriented electric dipole moment by the action of a local field E'. The external measurement proceeds in an applied field E and relative to the dielectric constant or permittivity of vacuum ϵ_o; $N\alpha$ has the dimension "permittivity." Hence, the polar response of a material is measured by the dimensionless quantities, electric susceptibility X or relative

permittivity κ,

$$\chi \equiv \kappa - 1 = \frac{P}{\epsilon_o E} . \tag{3}$$

Polarization changes proceed with energy dissipation; thus, in a-c fields these quantities are complex, composed of charging and loss components:

$$\chi_1^* = \chi' - j\chi'' ,$$

$$\kappa^* = \kappa' - j\kappa'' . \tag{4}$$

In anisotropic materials, furthermore, they become direction-dependent, i. e. , expand into matrices of nine coefficients,

$$\chi = \begin{vmatrix} \chi_{11}^* & \chi_{12}^* & \chi_{13}^* \\ \chi_{21}^* & \chi_{22}^* & \chi_{23}^* \\ \chi_{31}^* & \chi_{32}^* & \chi_{33}^* \end{vmatrix} . \tag{5}$$

Molecular analysis identifies the polarizability as stemming from electronic, atomic, and dipolar contributions, written schematically as

$$N\alpha = N_e\alpha_e + N_a\alpha_a + N_d\alpha_d + N_s\alpha_s. \tag{6}$$

Actually these effects are not independent of each other but come into play with very different time constants: the electronic polarizability α_e adjusts instantaneously (i. e. , with optical response frequencies) to the nuclear positions; the displacement of the nuclei, contained in the atomic polarizability α_a, is correlated to the infrared frequencies of the phonon spectra; the orientation of dipolar groups, responsible for the polarizability term α_d, appears in condensed phases normally as a relaxation spectrum in the electric range (d-c to millimeter waves); finally, quasi-dipolar phenomena are caused by the displacement of mobile charge carriers over larger distances, leading to a space-charge distortion of the applied field expressed by the polarizability term α_s. Since this piling up of charges may be due to electronic or ionic carriers, ranging in mobility all the way from thermally activated jumping processes to free band conduction of electrons and holes in semiconductors, space-charge polarization appears in various disguises: from "frozen-in" charges of electrets with time constants of years to the parametric response of semiconductor diodes still operative in the infrared.

Any one of the four polarization contributions of Eq. 6 can originate high-dielectric-constant effects, and the first three may cause ferroelectricity. In the present project we are primarily concerned with electronic and atomic polarization

phenomena, because they dominate in
ionic materials of high-temperature
stability and promise inherently low loss
in the electrical range. Since our Labo-
ratory had done extensive research on
rutile and ferroelectrics of the perovskite
type, these dielectrics were made the
central issue. However, as will become
apparent, even in these materials the
other two types of polarization enter in de-
vious ways, and excursions to additional
types of dielectrics proved indicated.

Identification of Problems

"Identification of decisive phenom-
ena and development of materials and
instrumentation for their thorough investi-
gation," these are generalities garnishing
many a research program. Underneath
such covering phrases proceeds - part-
ly by intuition - the search for a defini-
tion of the fundamental questions we actual-
ly want to ask and answer. This, in essence, was our line of reasoning:

Fig. 1. Temperature dependence of the
dielectric constant for various cubic
crystals and rutile (γ = 10 Mc/sec).

With increasing dielectric constant, the temperature coefficient of the per-
mittivity for polar materials switches from positive via neutral to strongly negative
values. This sequence was measured in our Laboratory, for example, on TiO_2
and the alkaline earth titanates during the war[1] and confirmed more accurately
some years ago on ceramics and single crystals[2] (Fig. 1 and Table 1). The phe-
nomenon obviously reflects the action of internal coupling effects which - under
proper conditions - lead to the Curie-Weiss law and the onset of ferroelectricity.

That law, derived by Weiss[3] for the explanation of ferromagnetism and
extended to polar molecules by Debye,[4] is normally based on two assumptions:
The applied field E is increased to a locally acting field E' (cf. Eq. 1) by a positive
feedback term proportional to the polarization P,

1) A. von Hippel and co-workers, N. D. R. C. Rep. VII, August, 1944.

2) A. von Hippel and W. B. Westphal, Tech. Rep. 145, Lab. Ins. Res., Mass.
   Inst. Tech., December, 1959.

3) P. Weiss, J. phys. 6, 667 (1907).

4) P. Debye, "Polar Molecules," Chemical Catalog Co., New York, 1929.

3

Table 1. Dielectric constants and their temperature coefficients for various cubic crystals and rutile at $150^\circ C$.

Crystal	κ'	$\frac{d\kappa'}{dT}$	$\frac{1}{\kappa'}\frac{d\kappa'}{dT}$
KCl	4.78	+0.0017	+0.00035
TlBr	30.0	-0.0038	-0.00012
TiO_2	80	-0.048	-0.00059
TiO_2	157	-0.12	-0.00076
$CaTiO_3$	146	-0.19	-0.0013
$SrTiO_3$	220	-0.49	-0.0022
$BaTiO_3$	3600	-53	-0.0147

$$\vec{E'} = \vec{E} + w \frac{\vec{P}}{\epsilon_o} ; \tag{7}$$

the polarizability per unit volume (cf. Eq. 2) furthermore varies inversely proportional to the temperature (Curie's law),

$$N\alpha = \frac{C}{T} . \tag{8}$$

According to Eqs. 1, 7, and 8, the susceptibility (Eq. 3) then obeys the Curie-Weiss law

$$X = \frac{\frac{N\alpha}{\epsilon_o}}{1 - w\frac{N\alpha}{\epsilon_o}} = \frac{\frac{T_c}{w}}{T - T_c} ; \tag{9}$$

it becomes infinite at the Curie temperature

$$T_c = \frac{wC}{\epsilon_o} , \tag{10}$$

when a self-alignment of the elementary dipole moments takes place.

This formalistic treatment has elements that are highly suspect. The phenomenon appears triggered by the external field E, while actually this is a sensing field, tracing the onset of a spontaneous phase transition by susceptibility measurements. The Curie law, furthermore, has a clear molecular meaning for the orientation of dipole molecules in gases,[5] but for crystals it is an empirical

5) Cf. A. von Hippel, "Dielectrics and Waves," John Wiley and Sons, New York, 1954.

4

ad hoc statement disguising our ignorance about the origin of the temperature dependence and its correlation to the various polarization effects. Finally, the feedback term in Eq. 7 was originally derived as the ordering action exercised by the long-range dipolar chain system of a polarized medium. When short-range order effects of individual polar groups can be neglected - as in randomized media or diatomic cubic crystals - the feedback field acts with a coupling factor

$$w = \frac{1}{3}. \tag{11}$$

This local field E' is known as the Clausius-Mosotti field and the feedback term as the Lorentz correction. For our cubic perovskites, however, a plot of the inverse susceptibility as function of temperature (Fig. 2),

$$\frac{1}{X} = \frac{w}{T_c} T - w, \tag{12}$$

reveals that the feedback term here is extremely small (Table 2). Hence, both the importance of the long-range field and the origin of the Curie-Weiss law are in doubt.
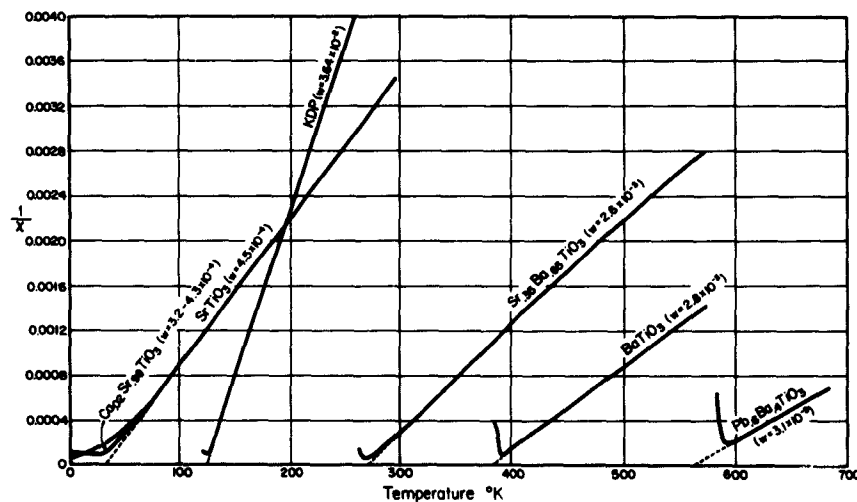
Fig. 2. Inverse susceptibility of various cubic perovskites and potassium dihydrogen phosphate.

With this, one set of basic questions has been isolated concerned with the pre-stages of ferroelectricity: what is the interpretation of the temperature dependence of the permittivity? Which parameters enter into the theory? And how can they be measured? (Measurements in this case require not only the development of new instrumentation but also better fabrication techniques for materials, as Fig. 3 testifies.) How essential is a long-range feedback field for the onset

Table 2. The Curie-Weiss law factors for various
ferroelectrics $1/\chi = [(w/T_c)T - w]$.

Material	T_c	w	w/T_c
$SrTiO_3$, crystal	37	4.5×10^{-4}	1.2×10^{-5}
$SrTiO_3$, ceramic	33	4.4×10^{-4}	1.3×10^{-5}
$Ca_{0.02}Sr_{0.98}TiO_3$	28-33	$3.2-4.3 \times 10^{-4}$	$1.16-1.31 \times 10^{-5}$
$Ba_{0.65}Sr_{0.35}TiO_3$	271	2.6×10^{-3}	9.6×10^{-6}
$BaTiO_3$, ceramic	383	2.8×10^{-3}	7.3×10^{-6}
$Ba_{0.4}Pb_{0.6}TiO_3$	562	3.1×10^{-3}	5.6×10^{-6}
KH_2AsO_4	86	2.75×10^{-2}	3.2×10^{-4}
KH_2PO_4	123	3.64×10^{-2}	2.95×10^{-4}
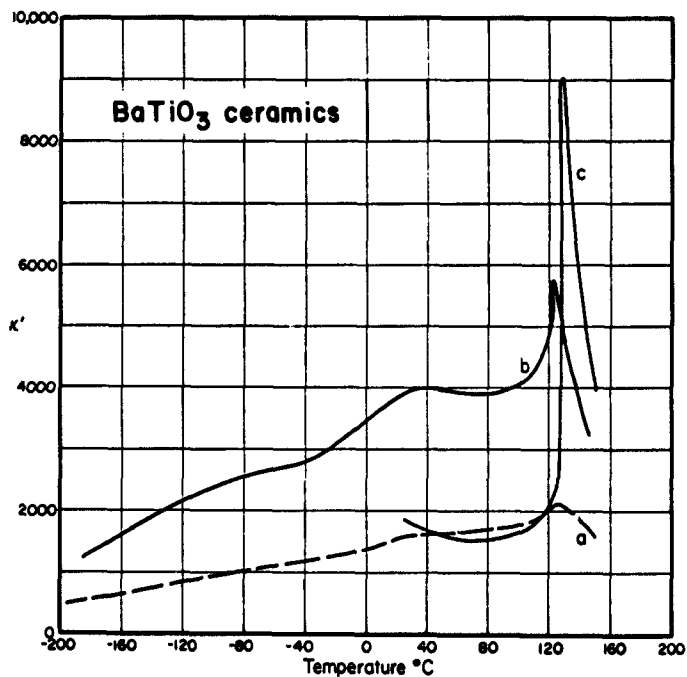
Fig. 3. Effects of initial particle size and grain growth
on dielectric constant of $BaTiO_3$. Hot-pressed
(a) from Laboratory powder $\sim 1\ \mu$; (b) from com-
mercial powder 1-20 μ; (c) same as (b) but hot-
sintered with consequent large grain growth.

6

of ferroelectricity ? Is the polarity ensuing at the phase transition perhaps an accidental by-product and the transformation completely directed by short-range-order terms ? In subsequent sections we will deal with these problems in detail.

When a crystal approaches a ferroelectric (or antiferroelectric) transition, its lattice distorts to lower symmetry. Polar axes develop due to nucleation and growth of dipolar order. Such axes have the choice of at least two opposite directions; for cubic crystals six equivalent $[100]$, eight $[111]$, and 12 $[110]$ directions offer themselves. Hence, the nucleation of order must be a time-consuming process of statistical organization before a domain pattern emerges. The problem arises of observing this latent period and of speeding up the choice by favoring a special orientation through mechanical strain or even by limiting it to a special polar direction through a biasing field.

Fig. 4. Frequency response of BaTiO$_3$, showing in succession the relaxation spectrum of domain-wall motion (pronounced at high field strength) and that of polar-axis rotation.

Once a ferroelectric state is established, its frequency response becomes an important problem. Various aspects of this phenomenon have been studied previously. The first measurements on BaTiO$_3$ ceramics[6] established - in analogy to ferromagnetics - two principal dispersion regions: a lower one caused by domain-wall motion and a higher one indicating disappearance of the ferroelectric response beyond the microwave range (Fig. 4). Measurements on single crystals, prepolarized normal to the electric field ("c" plates) but obviously still containing an antiparallel domain pattern, testified that the "small-signal" response characteristic for low frequencies[7] is still preserved in the microwave region[8] (Fig. 5).

6) A. von Hippel and W. B. Westphal, Annual Report - 1948 Conference on Electrical Insulation, National Research Council, Washington, D. C., March 15, 1949, p. 78; J. G. Powles and W. Jackson, Proc. Inst. Elec. Engrs. 96, Pt. 3, 383 (1949); A. von Hippel, "Molecular Science and Molecular Engineering," The Technology Press of M. I. T. and John Wiley and Sons, New York, 1959, p. 274.

7) W. J. Merz, Phys. Rev. 75, 687 (1949).

8) T. S. Benedict and J. L. Durand, Phys. Rev. 109, 1091 (1958); J. Fousek, Czechoslov. J. Phys. 9, 172 (1959).
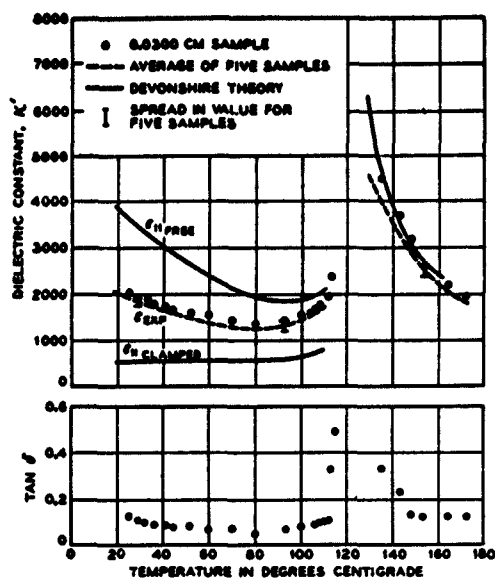
Fig. 5.

Small-signal dielectric constant at 24 kMc/sec as function of temperature for $BaTiO_3$ single crystals. Solid lines give theoretical values from Devonshire;[9] dashed line gives average value for the five crystals used; the points are those obtained for the "best" of the crystals used. Tan δ vs. temperature for "best" crystal. (After Benedict and Durand.[8])
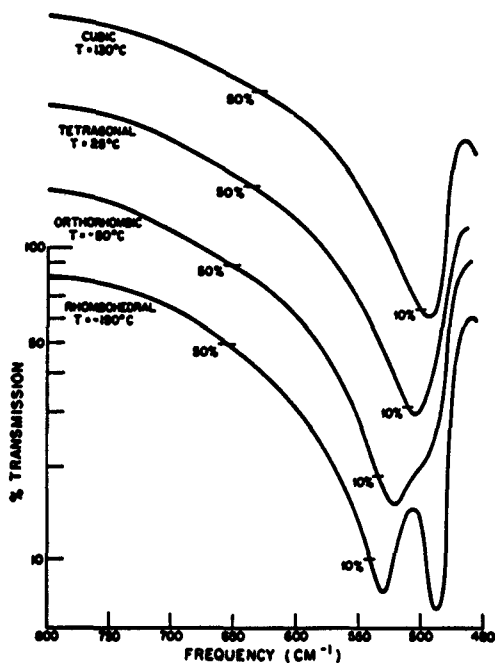
Fig. 6.

The infrared-absorption spectra of single-crystal $BaTiO_3$ (1.5 μ thick) for the cubic, tetragonal, orthorhombic, and rhombohedral phases.

9) A.F. Devonshire, Phil. Mag. [7] **42**, 1065 (1951).

An infrared study on $BaTiO_3$ above and below the Curie point showed[10] that the phase transition from cubic to tetragonal affected the two bands accessible at that time only as expected from the change in crystal symmetry; the great change in polarization caused by the onset of ferroelectricity went unnoticed (Fig. 6). The disappearance of the ferroelectric response was thus bracketed between the micro-wave region and these bands and could only be clarified by penetrating into the far infrared with new techniques.

At these ultrahigh frequencies a crystal of normal size acts "clamped," i.e., a mechanical distortion of its shape has no time to come into play. In the lower frequency range the electromechanical coupling can freely respond in de-formation, piezoelectric resonance effect may build up, domain walls can nucleate and move, and hysteresis loops can be traversed. Since here is the main range of applications for ferroelectrics, a large amount of research has been done on such phenomena.[11] At present, the losses of ferroelectrics are still too high, i.e., the hysteresis loops too wide, for many uses where ferromagnetics offer competition. The question is - how far can this situation be altered ?

Obviously, the problems enumerated cannot really be solved without a deeper understanding of the effects of cation and anion substitutions in the perov-skites. The present work is limited mainly to oxide compounds of the general designation ABO_3 with cation substitution in the A and B sites. Introduction of ions with magnetic moments had the additional goal of creating ferroelectrics with interesting magnetic properties.

Finally, the transfer of charge carriers through high-dielectric-constant materials continued to provide puzzles of great theoretical and practical interest.

Temperature Coefficient of the Dielectric Constant
The temperature coefficient of the dielectric constant with its trend from positive to strongly negative for increasing values of κ' (cf. Fig. 1) is measured at constant pressure. Thermodynamically, this coefficient is correlated to the temperature coefficient at constant volume as

$$\left(\frac{\partial \kappa'}{\partial T}\right)_p = \left(\frac{\partial \kappa'}{\partial T}\right)_V + \left(\frac{\partial \kappa'}{\partial V}\right)_T \left(\frac{\partial V}{\partial T}\right)_p \quad . \tag{13}$$

On the right side of this equation enters the coefficient of thermal expansion

$$\gamma = \frac{1}{V}\left(\frac{\partial V}{\partial T}\right)_p \quad . \tag{14}$$

10) J. T. Last, Phys. Rev. 105, 1740 (1957).

11) Cf., e.g., the recent survey by W. J. Merz, "Ferroelectricity" in "Progress in Dielectrics," Vol. 4, J. B. Birks and J. Hart, Eds., Academic Press, New York, 1962, p. 101.

Vice versa, if the temperature coefficient of the dielectric constant is measured at constant volume

$$\left(\frac{\partial \kappa'}{\partial T}\right)_V = \left(\frac{\partial \kappa'}{\partial T}\right)_P + \left(\frac{\partial \kappa'}{\partial p}\right)_T \left(\frac{\partial p}{\partial T}\right)_V , \qquad (15)$$

the compressibility

$$\beta = -\frac{1}{V}\left(\frac{\partial V}{\partial p}\right)_T \qquad (16)$$

is also involved, since

$$\left(\frac{\partial p}{\partial T}\right)_V = -\left(\frac{\partial p}{\partial V}\right)_T \left(\frac{\partial V}{\partial T}\right)_P = +\frac{\gamma}{\beta} . \qquad (17)$$

It follows that the volume and pressure coefficient of the dielectric constant at constant temperature are interrelated as

$$V\left(\frac{\partial \kappa'}{\partial V}\right)_T = -\frac{1}{\beta}\left(\frac{\partial \kappa'}{\partial p}\right)_T . \qquad (18)$$

The pair of variables, experimentally adjustable in the case of solid dielectrics and therefore chosen as the independent one, are temperature T and pressure p; effects relating to constant volume or primary volume change have to be calculated. Hence we rearrange our equations, placing on the right the quantities accessible to direct determination:

$$\left(\frac{\partial \kappa'}{\partial T}\right)_V = \left(\frac{\partial \kappa'}{\partial T}\right)_P + \left(\frac{\partial \kappa'}{\partial p}\right)_T \frac{\gamma}{\beta} ,$$

$$\left(\frac{\partial \kappa'}{\partial V}\right)_T = \frac{\left(\frac{\partial \kappa'}{\partial T}\right)_P - \left(\frac{\partial \kappa'}{\partial T}\right)_V}{V\gamma} . \qquad (19)$$

Thus there are to be measured: the temperature coefficient of the dielectric constant at constant pressure, its pressure coefficient at constant temperature, and - in addition - the volume, thermal expansion coefficient, and compressibility of the sample.

This experimental information has to be interpreted by considering the interplay of several effects:

1) Thermal expansion of the sample reduces the amount of polarizable material per unit volume, hence P. This decrease of X proportional to the density of the material is obviously a small negative contribution to the temperature coefficient, not sufficient even to upset the positive trend for ionic crystals of low dielectric constant.

10

2) Thermal expansion changes the overlap of the electronic wave functions and with it the splitting and competition of the molecular orbitals which determine the short-range-order structure of the crystal lattice. In the alkali halides with their rare-gas-shell ions the main effect of the overlap must be an octahedral deformation of the electron-cloud structure of the anions in the cube-edge directions for the rock-salt type (Fig. 7), or a bonding extending to the eight cation neighbors in space-diagonal directions for the CsCl structure. Expansion means reduction of this predistortion which stiffened the electron clouds against the polarizing influence of the external field. Hence, polarizability should increase with temper-

Fig. 7. Predistortion of Cl⁻ in NaCl.

ature and a positive temperature coefficient of the susceptibility should result, as observed for the alkali halides. The octahedrally bonded cations in rutile and the perovskites, on the other hand, have empty 3d shells and a complex competition between molecular orbitals might be expected as discussed in a later section.

3) The preceding description took a static point of view, based on the average position of the lattice ions. Actually, the nuclei make anharmonic oscillations, the overlap effect is observed as a dynamic averaging action, and the system moves with rising temperature toward larger thermal disorder. The statement "an increase of pressure is equivalent to a decrease of temperature" takes only the static situation into account and is obviously incorrect. We have to analyze the influence of thermal agitation both on the polarizability itself and on the entropy system, since the thermal-noise spectrum of the phonons interferes with the dipolar ordering tendency of the polarization and its preference for special phonon modes.

Attempts of Analysis

If one assumes the local field expression of Eq. 7 as valid and the feedback factor w constant, the susceptibility can be expressed as a function of Nα (cf. Eq. 9)

$$ \chi = \frac{\dfrac{N\alpha}{\epsilon_o}}{1 - w\dfrac{N\alpha}{\epsilon_o}} \cong \chi(N\alpha) . \tag{20} $$

Its temperature dependence at constant pressure becomes

11

$$\left(\frac{\partial \chi}{\partial T}\right)_p = N\alpha \frac{d\chi}{d(N\alpha)} \left[\frac{1}{N}\left(\frac{\partial N}{\partial T}\right)_p + \left(\frac{d\alpha}{dT}\right)_p\right] . \qquad (21)$$

Let N_o designate the total number of dipoles in a sample of volume V, or

$$N = \frac{N_o}{V} ; \qquad (22)$$

the first term in the brackets is obviously the negative volume of coefficient of thermal expansion (cf. Eq. 14),

$$\gamma = \frac{1}{V}\left(\frac{\partial V}{\partial T}\right)_p = -\frac{1}{N}\left(\frac{\partial N}{\partial T}\right)_p . \qquad (23)$$

The polarizability α and its temperature coefficient are to be investigated as function of volume and temperature,

$$\alpha = \alpha(V, T); \qquad (24)$$

$$\left(\frac{\partial \alpha}{\partial T}\right)_p = \left(\frac{\partial \alpha}{\partial V}\right)_T \left(\frac{\partial V}{\partial T}\right)_p + \left(\frac{\partial \alpha}{\partial T}\right)_V . \qquad (25)$$

The temperature coefficient of the susceptibility becomes therefore the sum of three effects:

$$\left(\frac{\partial \chi}{\partial T}\right)_p = N\alpha \frac{d\chi}{d(N\alpha)}\left[-\gamma + \frac{\gamma V}{\alpha}\left(\frac{\partial \alpha}{\partial V}\right)_T + \frac{1}{\alpha}\left(\frac{\partial \alpha}{\partial T}\right)_V\right]. \qquad (26)$$

Thermal expansion dilutes the dielectric - a small negative contribution; the volume and temperature dependence of α are the real issue.

From Eq. 20 it follows that the expression in front of the bracket in Eq. 21 can be written

$$N\alpha \frac{d\chi}{d(N\alpha)} = \frac{\chi}{1 - w\frac{N\alpha}{\epsilon_o}} = \frac{\chi(\chi + \frac{1}{w})}{\frac{1}{w}} . \qquad (27)$$

If we assume the feedback factor $w = 1/3$ - the Lorentz local field - Eq. 27 can be rewritten for the dielectric constant as

$$N\alpha \frac{d\kappa'}{d(N\alpha)} = \frac{(\kappa' - 1)(\kappa' + 2)}{3} . \qquad (28)$$

Comparison of Eqs. 13 and 26 - with the approximation Eq. 28 - lead to the molecular formulation of Eqs. 19 for the temperature- and volume-dependent coefficients of the dielectric constant:

12

$$\left(\frac{\partial \kappa'}{\partial T}\right)_V = \frac{(\kappa' - 1)(\kappa' + 2)}{3T} \left[\frac{T}{a}\left(\frac{\partial a}{\partial T}\right)_V\right];$$

(29)

$$\left(\frac{\partial \kappa'}{\partial V}\right)_T = \frac{(\kappa' - 1)(\kappa' + 2)}{3V} \left[-1 + \frac{V}{a}\left(\frac{\partial a}{\partial V}\right)_T\right].$$

Interpretation of $(\partial a/\partial V)_T$, Based on a Model of Born and Huang[12]

Given an ionic diatomic lattice consisting of point charges $\pm Ze$ of the electronic polarizabilities a_+ and a_-, the electronic dipole moments are visualized as point dipoles located at the position of the nuclei. The positive and negative Bravais sublattices vibrate against each other in harmonic oscillations (optical modes) with wavelengths long compared with the nearest-neighbor distance r_0 between cation and anion; the electronic polarization follows instantaneously. The locally acting field is the Clausius-Mosotti field (cf. Eqs. 7 and 11):

$$E' = E + \frac{\vec{P}}{3\epsilon_0} = \frac{\vec{E}}{3}(\kappa' + 2).$$

(30)

The polarization results from the action of N ion pairs per unit volume contributing ionic dipole terms Zeu_+ and Zeu_- (where u_+ and u_- designate the displacement of the ionic charges) and of N electronic dipoles produced by the polarizing effect of the local field

$$P = N\left[Ze(u_+ - u_-) + (a_+ + a_-)E'\right].$$

(31)

The electronic polarizabilities can be determined from the dielectric constant at optical frequencies (κ'_∞) (cf. Eqs. 1, 3, and 30) as

$$\frac{N(a_+ + a_-)}{3\epsilon_0} = \frac{(\kappa'_\infty - 1)}{(\kappa'_\infty + 2)}.$$

(32)

The relative displacement of the positive against the negative ions, $u_+ - u_-$, causes the overlap potential to produce restoring forces $-k(u_+ - u_-)$ and $k(u_+ - u_-)$, respectively; in addition, the local field acts on the ionic dipole moments as ZeE' and $-ZeE'$; hence, the equations of motion for the two ion types are

$$m_+ \ddot{u}_+ = -k(u_+ - u_-) + ZeE',$$
$$m_- \ddot{u}_- = k(u_+ - u_-) - ZeE'.$$

(33)

By multiplying with m_- and m_+ respectively, subtracting the two equations and

12) Cf. M. Born and K. Huang, "Dynamical Theory of Crystal Lattices," Clarendon Press, Oxford, 1954, pp. 82 ff. and 104 ff.

13

dividing by $m_+ + m_-$, the oscillator equation for the reduced mass results:

$$m_r(\ddot{u}_+ - \ddot{u}_-) = -k(u_+ - u_-) + ZeE', \qquad (34)$$

with

$$m_r = \frac{m_+ m_-}{m_+ + m_-} \quad .$$

The effective field E' itself depends on $u_+ - u_-$ (cf. Eqs. 30 and 31) as

$$E' = \frac{E + \dfrac{N}{3\epsilon_0} Ze(u_+ - u_-)}{1 - \dfrac{N}{3\epsilon_0}(a_+ + a_-)} \quad ; \qquad (35)$$

hence,

$$m_r(\ddot{u}_+ - \ddot{u}_-) = \left[-k + \frac{\dfrac{N(Ze)^2}{3\epsilon_0}}{1 - \dfrac{N}{3\epsilon_0}(a_+ + a_-)} \right] (u_+ - u_-) + \frac{ZeE}{1 - \dfrac{N}{3\epsilon_0}(a_+ + a_-)} \quad . \quad (36)$$

By introducing the parameter

$$w = (Nm_r)^{1/2}(u_+ - u_-), \qquad (37)$$

the oscillator equation for the optical vibration of the lattice ions can be re-written

$$\ddot{w} + \left[\frac{k}{m_r} - \frac{\dfrac{N(Ze)^2}{m_r 3\epsilon_0}}{1 - \dfrac{N}{3\epsilon_0}(a_+ + a_-)} \right] w = \frac{ZeE(\dfrac{N}{m_r})^{1/2}}{1 - \dfrac{N}{3\epsilon_0}(a_+ + a_-)} \quad . \qquad (38)$$

Without external field, the lattice vibration has the reduced resonance frequency (due to polarization)

$$\omega_0' = \left[\frac{k}{m_r} - \frac{\dfrac{N(Ze)^2}{m_r 3\epsilon_0}}{1 - \dfrac{N}{3\epsilon_0}(a_+ + a_-)} \right]^{1/2} \quad , \qquad (39)$$

with $\omega_0 \cong \sqrt{k/m_r}$, the resonance frequency caused by the short-range restoring force.

The parameter w allows to combine Eqs. 38 and 31 in the symmetrical form:

$$w = b_{11}w + b_{12}E$$
$$P = b_{21}w + b_{22}E \quad . \qquad (40)$$

14

The coefficients (in view of Eq. 32) represent:

$$b_{11} = -\omega_o'^2, \quad b_{12} = b_{21} = \frac{Ze\left(\frac{N}{m_r}\right)^{1/2}(\kappa_\infty' + 2)}{3}$$

$$b_{22} = \epsilon_o(\kappa_\infty' - 1). \tag{41}$$

For a periodic, undamped oscillation of frequency ω, the steady-state solution for the polarization P is obtained from Eqs. 40 (by eliminating w) as

$$\vec{P} = \left(b_{22} + \frac{b_{12}b_{21}}{-b_{11} - \omega^2}\right)\vec{E}; \tag{42}$$

hence, the susceptibility χ becomes

$$\frac{P}{\epsilon_o E} = (\kappa_\infty' - 1) + \frac{(Ze)^2\left(\frac{N}{m_r}\right)(\kappa_\infty' + 2)^2}{9\epsilon_o(\omega_o'^2 - \omega^2)}. \tag{43}$$

The infrared resonance of the diatomic lattice at ω_o' causes a difference between static and optical dielectric constant

$$\kappa_s' - \kappa_\infty' = (\kappa_\infty' + 2)^2\frac{N(Ze)^2}{\epsilon_o 9m_r\omega_o'^2}. \tag{44}$$

Thus Eq. 43 can be rewritten in the well-known resonance-dispersion formulation for the dielectric constant (absorption neglected)

$$\kappa' = \kappa_\infty' + \frac{\kappa_s' - \kappa_\infty'}{1 - \left(\frac{\omega}{\omega_o'}\right)^2}. \tag{45}$$

Eqs. 40 were originally derived by Huang[13] and Eq. 44 by Szigeti.[14]

The volume dependence of the dielectric constant at constant temperature (Eq. 29) on the basis of this linear oscillator model is

$$\left(\frac{\partial\kappa'}{\partial V}\right)_T = \left(\frac{\partial\kappa_\infty'}{\partial V}\right)_T + \left(\frac{\partial}{\partial V}\right)_T\left\{\frac{\kappa_s' - \kappa_\infty'}{1 - \left(\frac{\omega}{\omega_o'}\right)^2}\right\}. \tag{46}$$

13) K. Huang, Proc. Roy. Soc. (London) A208, 352 (1951).
14) B. Szigeti, ibid. A204, 52 (1950).

15

Equation 46 allows to express the volume dependence of the electronic polarizability by the optical dielectric constant and its volume coefficient:

$$\Lambda_o \equiv \frac{V}{\alpha_e}\left(\frac{\partial \alpha_e}{\partial V}\right)_T = \left(\frac{\partial \kappa_\infty'}{\partial V}\right)_T \frac{3V}{(\kappa' - 1)(\kappa' + 2)} . \qquad (47)$$

Λ_o is known as the (optical) strain-polarizability constant.

From Eqs. 32, 39, and 44 follows the relation for the reststrahl frequency ω_o':

$$\omega_o'^2 = \frac{k}{m_r} \frac{(\kappa_\infty' + 2)}{(\kappa_s' + 2)} . \qquad (48)$$

It can serve to determine the force constant k that holds the ions to their equilibrium positions, by measuring ω_o', κ_s', κ_∞' and knowing the reduced mass m_r. On the other hand, the force constant k is inversely proportional to the compressibility β of Eq. 16. A calculation based on the overlap potential gives the result[12]

$$\frac{1}{\beta} = \frac{Cn\, r_o^2 N}{3} k, \qquad (49)$$

where Cn is the coordination number and r_o the distance between nearest-neighbor ions. Hence, by eliminating k in Eq. 49 with the help of Eq. 48, a relation between directly measurable quantities results, as derived by Szigeti:[14]

$$\frac{1}{\beta} = \frac{Cn\, m_r\, r_o^2 N}{3} \left(\frac{\kappa_s' + 2}{\kappa' + 2}\right) \omega_o'^2 . \qquad (50)$$

This simple linear oscillator model for the volume dependence of the dielectric constant does not prove very satisfactory, as shown by Fuchs[15] in detail. Ad hoc corrections have to be introduced - an effective charge (se) in place of the electronic charge e and a temperature coefficient of this effective charge - to produce reasonable agreement between theory and existing data.

Refinement of the Discussion of $(\partial \alpha / \partial V)_T$, Based on the Shell Model of Dick and Overhauser[16]

The anions are considered as consisting of a positive core coupled by an isotropic force constant to a negative shell representing the outer electrons. This assumption changes the equations of motion (Eqs. 33) as follows:

15) R. Fuchs, Tech. Rep. 167, Lab. Ins. Res., Mass. Inst. Tech., Nov., 1961.

16) B. G. Dick, Jr., and A. W. Overhauser, Phys. Rev. 112, 90 (1958).

$$m_+ \ddot{u}_+ = k_+(u_s - u_+) + Z_+ eE' ,$$

$$m_c \ddot{u}_c = k_c(u_s - u_c) + Z_c eE' , \qquad (51)$$

$$o = k_+(u_+ - u_s) + k_c(u_c - u_s) + Z_s eE' .$$

The subscripts +, c, and s refer to the cation, the core, and the shell of the anion, respectively. The first two equations describe the interactions cation to shell and positive core to shell, and the electrostatic action of the effective field E' on cation and core charge; the third equation specifies that the electronic shell is always in an equilibrium position relative to the instantaneous position of the nuclei. The interplay between cation and core (of the anion) is indirect, with the shell acting as intermediary.

Since the relative displacement of the two nuclei against each other is the directly measurable quantity to which also the previous model referred (cf. Eq. 34), Eqs. 51 are rewritten in reference to this distance $u_+ - u_c$ as:

$$-m_+ \ddot{u}_+ = k_+(u_+ - u_c) + k_+(u_c - u_s) - Z_+ eE' ,$$

$$-m_c \ddot{u}_c = k_c(u_c - u_+) + k_c(u_+ - u_s) - Z_c eE' , \qquad (52)$$

$$o = k_+(u_c - u_+) + (k_c + k_+)(u_s - u_c) - Z_s eE' .$$

By eliminating, with the help of the third equations, all displacement terms other than $u_+ - u_c$, the two equations of motion result:

$$m_+ \ddot{u}_+ = -k'_+(u_+ - u_c) + Z'e\vec{E}' ,$$

$$m_c \ddot{u}_c = k'_+(u_+ - u_c) - Z'e\vec{E}' , \qquad (53)$$

where

$$k'_+ = \frac{k_c k_+}{k_c + k_+} \text{ and } Z' = Z_+ + \frac{k_+ Z_s}{k_c + k_+} \qquad (54)$$

and where we have used $Z_+ + Z_c + Z_s = 0$. Equations 53 are quite analogous to Eqs. 33 and can again be combined into one equation for the reduced mass (since $m_c \simeq m_-$):

$$m_r(\ddot{u}_+ - \ddot{u}_c) = -k'_+(u_+ - u_c) + Z'eE' ; \qquad (55)$$

i. e., the shell model has introduced in place of one force constant k two force constants k_+ and k_c combined in k'_+ and in place of one charge number Z two charge numbers Z and Z_s as expressed by Z'.

Transversal and Longitudinal Optical Modes

The linear oscillator model of the previous sections is based on the following picture: An optical phonon mode - of wavelength long in comparison with the atomic distance - causes a displacement of the positive versus the negative partial Bravais lattice of a diatomic crystal and thus an atomic polarization proportional to the relative displacement of the undistorted sublattices (cf. Eq. 31). This atomic polarization produces a local field (Eq. 30) creating an instantaneous electronic polarization (Eq. 31). Atomic and electronic polarizations, in feedback action (Eq. 30), increase the atomic displacement, i.e., weaken the restoring force and lower the mechanical resonance frequency ω_o to ω_o' (Eq. 39).

This concept obviously refers to a normal "reststrahl" frequency mode, which - in reference to the propagation direction of an exciting electromagnetic wave - is a transversal mode. Thus Eq. 39, in view of Eq. 32 and by replacing k with k_+' and Z with Z' for the shell model, can be rewritten

$$\omega_T \equiv \omega_o' = \left[\frac{k_+'}{m_r} - \frac{N(\kappa_\infty' + 2)(Z'e)^2}{9m_r \epsilon_o} \right]^{1/2} \quad (\omega_o^2 - x^2)^{1/2}, \qquad (56)$$

where ω_o is the mechanical resonance frequency and x the lowering effect by polarization feedback coupling.

In addition to this transversal mode, Born and Huang and others introduce a longitudinal resonance frequency ω_L in reference to an applied external field E, but here some confusion arises. It is assumed that the polarization P which accompanies the wave mode (cf. Eq. 31) balances the external field; i.e.,

$$\vec{E} = -\frac{\vec{P}}{\epsilon_o} . \qquad (57)$$

The result is a "stiffening" of the longitudinal frequency beyond the mechanical resonance frequency:

$$\omega_L = \left[\omega_T^2 + \frac{N(\kappa_\infty' + 2)^2 (Z'e)^2}{9m_r \epsilon_o \kappa'} \right]^{1/2} = (\omega_o^2 + \frac{2}{\kappa_\infty'} x^2)^{1/2}. \qquad (58)$$

From Eq. 44 one obtains for the ratio of static to optical dielectric constant (when only electronic and atomic polarization exists)

$$\frac{\kappa_s'}{\kappa_\infty'} = 1 + \frac{N(\kappa_\infty' + 2)^2 (Z'e)^2}{9m_r \epsilon_o \kappa' \omega_T^2} . \qquad (59)$$

18

Thus the well-known relation results[17]

$$\frac{\kappa'_s}{\kappa'_\infty} = \left(\frac{\omega_L}{\omega_T}\right)^2 . \tag{60}$$

This method of introducing a longitudinal optical mode seems to be questionable. The difficulty stems from the identification of the polarization P accompanying a phonon wave with that produced by the external field (Eq. 57). These two phenomena have no direct connection. The sensing field E, normally applied, causes only a minute disturbance of the internal state of polarization, because the field energy placed by E across an elementary cell is very small compared with kT.

If one introduces the concept of a longitudinal and transversal optical mode in reference to an external field E, the static dielectric constant is measured parallel to the field; ω'_0 in Eq. 44 should therefore be replaced by ω_L, not by ω_T. In place of Eq. 60 one now obtains the relation

$$\frac{\kappa'_s}{\kappa'_\infty} = 2 - \left(\frac{\omega_T}{\omega_L}\right)^2 . \tag{61}$$

While Eq. 60 claims that the static dielectric constant becomes infinite when the transversal resonance frequency is pulled down to zero, Eq. 61 states that the static dielectric constant for $\omega_T = 0$ can only rise to twice the optical dielectric constant on account of the stiffening of the longitudinal mode - an abstruse result.

The concepts "longitudinal" and "transversal" can have a different connotation when the Bravais sublattices are not kept undistorted and the wavelength of the mode is smaller than the crystal dimensions. "Longitudinal" would now mean an end-on vibration resulting in compressions and dilations of the lattice-plane spacings, while "transversal" would refer to a shear wave with sidewise displacements of the partial lattices against each other. Obviously, the shear wave has the smaller restoring force and thus the lower frequency. However, this interpretation does not enter here, since the calculation was based on undistorted sublattices.

Explanation of the Onset of Ferroelectricity by Mode Pulling and the Difficulties of Cochran's Theory

The "softening" of the transversal optical mode by polarization (Eq. 56) and the rapid rise of the static dielectric constant, when this mode is lowered (Eq. 60), offer a tempting explanation for the onset of ferroelectricity. Cochran[18] has

17) R.H. Lyddane, R.G. Sachs, and E. Teller, Phys. Rev. 59, 673 (1941); cf. also M. Born and K. Huang, loc. cit., p. 86.

18) W. Cochran, Advances in Physics 9, 387 (1960).

developed this idea into an important theory by coupling Eq. 60 to the postulate of a proper temperature dependence for ω_T^2:

$$\frac{\omega_T^2}{\omega_0^2} = \gamma(T - T_c) \ . \tag{62}$$

The factor γ is akin to the volume coefficient of thermal expansion (Eq. 14) and ω_0 corresponds to the undisturbed mechanical resonance frequency of the preceding equations.

Equation 60 - as already pointed out - we consider disputable, but actually the theory is independent of it: As long as the transversal optical mode determines the static dielectric constant according to the dispersion equation (cf. Eqs. 44 and 45), a pulling down of ω_T to zero raises κ'_s to infinite. By combining Eq. 59 and Eq. 62, the Curie-Weiss law results in the form

$$\kappa'_s = \kappa'_\infty + \frac{(\kappa' + 2)x^2}{\omega_0^2 \gamma(T - T_c)} \ . \tag{63}$$

From Eq. 63, using Eq. 56, we get

$$\kappa'_s + 2 = (\kappa'_\infty + 2) \ \frac{\omega_T^2 + x^2}{\omega_T^2} \ , \tag{64}$$

which by using Eqs. 62 and 56 can be rewritten as

$$\kappa'_s + 2 = \frac{\kappa'_\infty + 2}{\gamma(T - T_c)} \ . \tag{65}$$

This leads to the temperature coefficient at constant pressure

$$\left(\frac{\partial \kappa'_s}{\partial T}\right)_p = - \frac{(\kappa'_\infty + 2)}{\gamma(T - T_c)} \ . \tag{66}$$

Cochran suggests that the truth of Eq. 62 is self-evident; Eq. 66, however, shows that this is not at all the case. A strong negative temperature coefficient of the static dielectric constant is prescribed by his equation, while actually the theory is first developed for a diatomic crystal of the alkali halide type where the coefficient is positive.

Cochran's theory continues very ingeniously. As is well known, the linear oscillator model is really not applicable, since thermal expansion of the lattice is caused by anharmonic forces, and the departure from the parabolic potential well

gives rise to a temperature-dependent polarizability. [19] Following Devonshire's theory, [9] Cochran introduces, in addition to the linear term of the restoring force (Eq. 55), a third- and fifth-order term of the relative displacement $u = u_+ - u_c$, but the polarizing force enlarging the displacement is assumed to remain linear. Hence the equation of motion becomes

$$m_r \ddot{u} = - \left[k_+' u + B u^3 + B' u^5 \right] + Z' e E' ,\qquad (67)$$

where (cf. Eqs. 36 and 32) for $E = 0$

$$Z' e E' = \frac{N(k_\infty' + 2)(Z'e)^2}{9 e_o} \, u .\qquad (68)$$

When the restoring and the linear displacing forces, divided by the reduced mass, are plotted as $f(u)$ (cf. Eq. 38), the difference in slope of the two characteristics at the origin equals ω_T^2, and the slope of the displacing force line is x^2 (Fig. 8). Furthermore, if the linear theory can still be used for discussion of the temperature dependence (i.e., if the restoring force characteristic remains unchanged by temperature),

$$\frac{x^2}{\omega_o^2 \gamma} = (T_c + \frac{1}{\gamma}) - T.\qquad (69)$$

The slope of the displacing-force line increases linearly with decreasing temperature. When the line intersects the restoring force characteristic so that the shaded areas above and below are equal, the two Bravais lattices can also oscillate in an equilibrium position mutually displaced by u_{tr}, and the free energy of the two phases are alike; hence, a "first-order" transition into a ferroelectric state can occur ($T_{tr} > T_c$). If the characteristics are so located that their tangents at the origin coincide before they intersect, the ferroelectric state is reached at T_c in a "second-order" transition.

Cochran's theory demands, since the static dielectric constant at the Curie point is very high ($\approx 10^4$) and k_∞' about 5 for soft materials of alkali halide structure, that near-cancellation of restoring and displacing force ($\omega_o^2 \approx x^2$) occurs, or (from Eqs. 62 and 63)

$$\omega_T \simeq \left(\frac{k' + 2}{k_s'} \, \omega_o \right)^{1/2} ; \quad \omega_T \approx \frac{1}{40} \, \omega_o;\qquad (70)$$

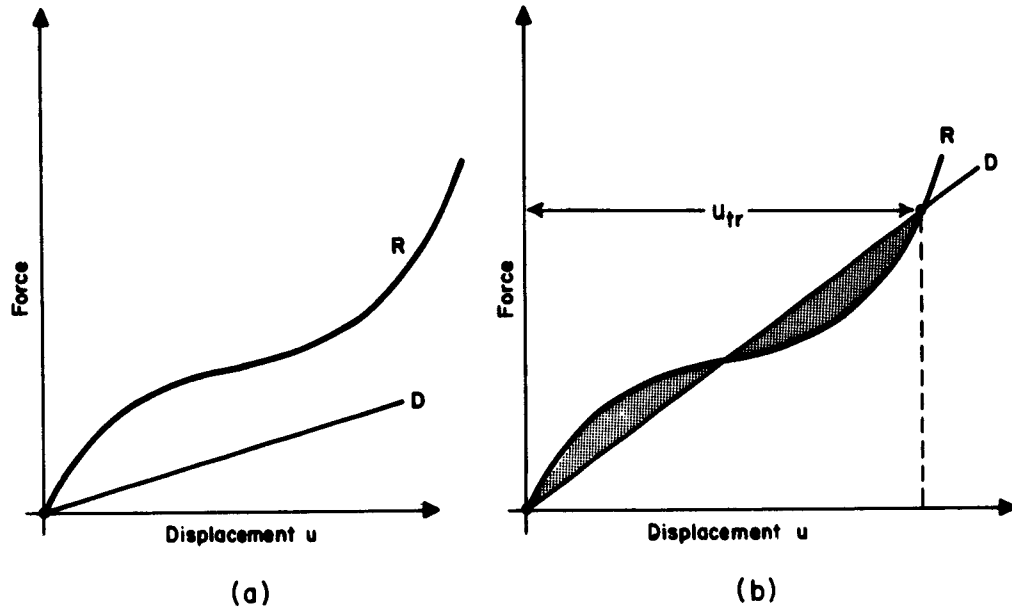19) F.C. Frank, Trans. Faraday Soc. 42, 251 (1946).

21

Fig. 8. Onset of ferroelectricity by mode pulling.
(a) Above transition temperature; (b) at
transition temperature. (R = restoring
force divided by m_r; D = displacement
force divided by m_r.) (After Cochran.[18])

a "reststrahl mode" located normally near 100 μ should be displaced to about 4 mm
wavelength! Such a tremendous softening of the basic reststrahl mode is hard to
credit. However, some experimental evidence for such an effect has been
claimed by observers who extrapolated their spectroscopic data through the still
poorly accessible far-infrared region with the help of the Kramers-Kronig
relation.[20]

     We do not believe in this type of mode pulling and are trying to check it
with direct interference spectroscopy. One reason which makes Eq. 70 especial-
ly suspect is that the calculation is based on the Lorentz factor 1/3. Actually, as
shown in Fig. 2 and Table 2, the experimentally measured coupling factor w is
smaller by two orders of magnitude. Hence, if the softening of the mode by the
Lorentz field could previously create a static dielectric constant 10^4, the same
polarization field of the phonon mode can now only provide $k'_s \approx 10^2$.

20) A. S. Barker, Jr., and M. Tinkham, Phys. Rev. 125, 1527 (1962); W. G. Spitzer,
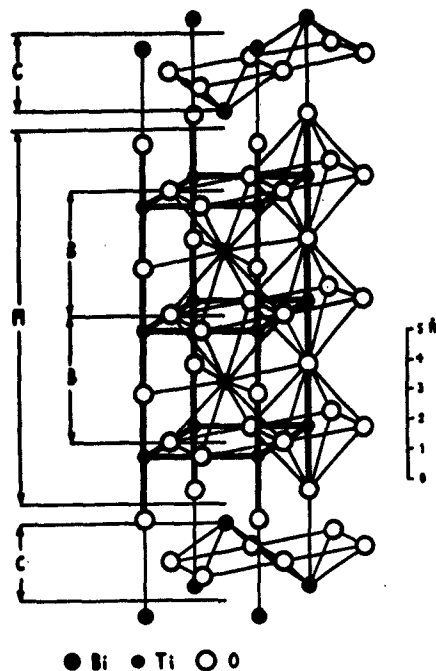   R. C. Miller, D. A. Kleinman, and L. E. Howarth, Ibid. 126, 1710 (1962).

Fig. 9.

One half of the pseudo-tetragonal unit cell of $Bi_4Ti_3O_{12}$ (from $z \simeq 0.25$ to $z \simeq 0.75$). A is the perovskite layer $Bi_2Ti_2O_{10}^{2-}$; C are the $Bi_2O_2^{2+}$ layers; and B the unit cells of the hypothetical perovskite structure $BiTiO_3$. (After Aurivillius.[21])

● Bi   ● Ti   O O

The small coupling factor discredits the whole concept that a long-range feedback field causes the onset of ferroelectricity. An additional support for this conclusion arises from quite different evidence: If the long-range action of a polarization wave is decisive, any interruption of the dipolar mode pattern by the insertion of layers into the lattice structure should impair the formation of the ferroelectric state. Actually, this is not the case: Figure 9 shows the lattice structure of the bismuth titanate $Bi_4Ti_3O_{12}$ according to Aurivillius.[21] It consists of layers of perovskite - two unit cells wide - separated by Bi_2O_2 layers. In addition to this interruption of the sequence, the perovskite sections are alternatively displaced sidewise by half a lattice parameter. Such stacking should make the development of a uniform long-range polarisation field practically impossible. Still, the compound proves ferroelectric[22] with a Curie temperature of about $643^\circ C$.

21) B. Aurivillius, Arkiv Kemi 58, 499 (1949).
22) E. C. Subbarao, Phys. Rev. 122, 804 (1961).

Feedback Coupling and the Origin of the Curie-Weiss Law

The preceding discussion of the Cochran model has led to some confusion. The mode-pulling effect as such stems from the linear oscillator model and concerns the volume dependence of the polarization at constant temperature $(\partial a/\partial V)_T$. The ad hoc introduction of the Curie-Weiss law (Eq. 62) switched the emphasis to a discussion of the temperature dependence of the polarization, to the third term $(\partial a/\partial T)_V$ of Eq. 26. It became clear that for ferroelectrics in the paraelectric range the Clausius-Mosotti field applies with a very small feedback factor w, which proves about temperature independent (cf. Fig. 2). This has some interesting consequences.

When the Curie-Weiss law holds in the form of Eq. 9, the temperature coefficient of the dielectric constant becomes

$$\frac{1}{\chi^2} \left(\frac{\partial \kappa'}{\partial T} \right)_p = - \frac{w}{T_c} . \tag{71}$$

If one plots w/T_c for ferroelectrics as $f(T_c)$, approximately a straight line results (Table 2, p. 6, and Fig. 10), i.e.,

$$\frac{w}{T_c} = a - bT_c . \tag{72}$$

A similar straight line has been found for $1/\kappa'^2(\partial \kappa'/\partial T)_p$ by Bosman and Havinga.[23] They use the fixed Lorentz feedback factor $1/3$, hence have no ready interpretation. Equation 72 and Fig. 10 explain that the feedback factor w depends on the Curie temperature as

$$w = aT_c - bT_c^2 . \tag{73}$$

The reason for this dependence must be found by molecular analysis.

Bosman and Havinga also measured the pressure dependence of the dielectric constant and, by using literature data for thermal expansion and compressibility, obtained a curve of the temperature dependence of the dielectric constant at constant volume (Fig. 11a). Our data, drawn for the feedback factor w in place of the constant Lorentz factor $1/3$ by substituting

$$(\kappa' - 1)(\kappa' + 2) \longrightarrow \frac{3\kappa'^2(1 + \frac{1}{\kappa'w})}{\frac{1}{w}} \longrightarrow 3\kappa', \text{ for } \kappa'w \ll 1, \tag{74}$$

are given in Fig. 11b. These characteristics make it clear that the temperature dependence of the polarizability represents the main effect for ionic crystals. It causes the switch from positive to negative temperature coefficient as one proceeds

23) A. J. Bosman and E. E. Havinga, Phys. Rev., in press. We are greatly indebted to the authors and to Dr. Jonkers for a preprint of this paper.
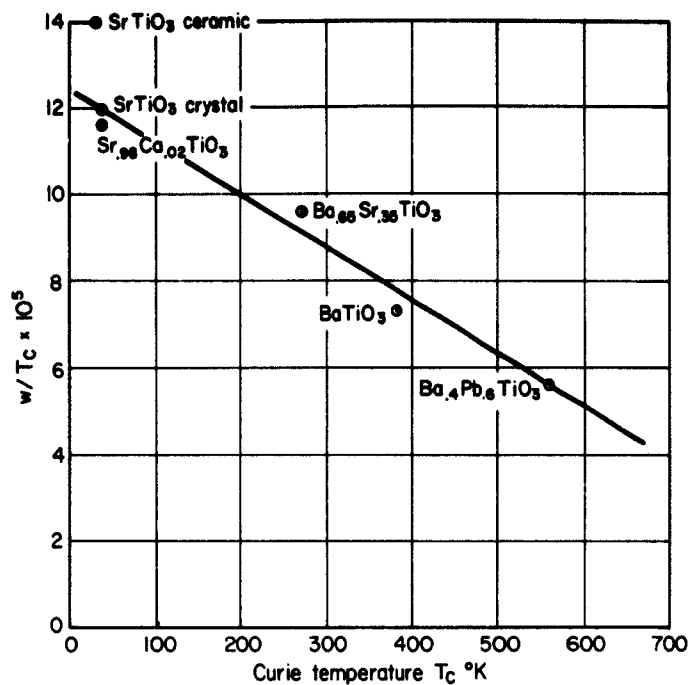
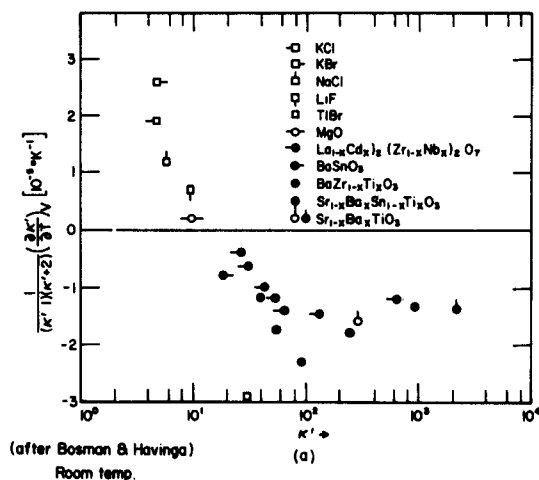Fig. 10. Curie-Weiss law factor w/T_c versus T_c for various perovskites.

(after Bosman & Havinga)
Room temp. (a) (b) (L.I.R.)
150 °C

Fig. 11a. The temperature dependence of the dielectric constant at constant volume as a function of κ' for a number of cubic compounds at room temperature. (After Bosman and Havinga.[23])
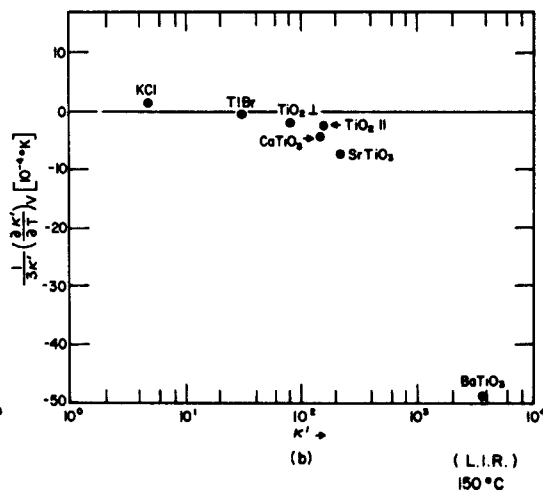
Fig. 11b. The temperature dependence of the dielectric constant at constant volume as function of κ' for a number of compounds at 150°C.

to materials of high dielectric constants. In the preceding section we demonstrated that this effect does not arise from the long-range ordering feedback field. The alternative is to make short-range-order terms responsible for the Curie-Weiss law and the onset of the ferroelectric state.

Ferroelectricity and Molecular Bonding

A ferroelectric may have a molecular lattice, in which whole polar groups align as observed for thiourea[24] and sodium nitrite.[25] In hydrogen-bonded structures, the proton positions may order and produce electric dipole systems - either directly or through the resulting deformation of connecting groups; potassium dihydrogen phosphate was the first case shown to polarize by such deformation.[26] In structures stabilized by water molecules, cases of polar alignment of these molecules may be expected.

In such situations, attention focuses first on the nearest-neighbor constellations and then on the over-all pattern into which these groups are inserted. In ionic lattices, in contrast, the crystalline arrays of Bravais lattices and sub-lattices have received the main attention, while the importance of the short-range molecular groupings, the constellations of tetrahedra, octahedra, etc., surrounding the cations, was practically lost. Obviously, the formation of a polar axis can only occur when the distortion is permitted by crystal symmetry as well as by the electron-pair bond structure of these nearest-neighbor surroundings. Since the preceding discussion has shown that the very small feedback factor w relegates the long-range ordering field of the polar phonon modes to secondary importance, the triggering cause for ferroelectric ordering must stem in this situation from the competition between various molecular bonds. The relative position of the competing energy states must change $\sim 1/T$ and cause the Curie law, when a ferroelectric phase transition is approached. The specificity of the phenomenon can thus be understood by the specific bond structure realized by the various cations in their anion surroundings and the polar distortion these bonds can enforce on the crystal symmetry.

24) A. Solomon and G. J. Goldsmith, Phys. Rev. 104, 1191 (1956).

25) S. Nomura, J. Phys. Soc. Japan 16, 2440 (1961).

26) J. C. Slater, J. Chem. Phys. 9, 16 (1941); B. C. Frazer and R. Pepinsky, Acta Cryst. 6, 273 (1953).

Mr. Nelson presents in the subsequent section a qualitative discussion of the possible molecular bonds in our perovskites. The temperature dependence of the competing energy terms and the detailed correlation between ferroelectricity and chemical composition will be derived in a future publication.

Ferroelectricity and the Chemical Bond in Perovskite-Type Oxides

The occurrence of ferroelectricity and antiferroelectricity in perovskite-type oxides is inadequately explained by the postulate of an ionic model. Such a model with its radius-ratio rules emphasizes the concept of a critical ionic radius at which rattling of cations within their octahedral oxide surroundings begins. A molecular-orbital approach provides additional insight into the nature of these distortions. If the 2s and one 2p orbitals of each O^{2-} ion are hybridized to provide two equivalent sp-directed ones to the octahedral-coordinated cations, the remaining two 2p orbitals are unchanged. When these 2p orbitals of all ligands become increasingly involved with only the cuboctahedral-coordinated cation of decreasing size, the cubic phase (e. g. , $BaTiO_3$ above $126^{o}C$, or $SrTiO_3$) or a slightly distorted variant (in which the framework of centrosymmetric octahedra pivots and tilts, e. g. , $CaTiO_3$) occurs. When, on the other hand, these orbitals on one, two, or three ligands become involved with the octahedral-coordinated cation, π bonds form and tetragonal, orthorhombic, and rhombohedral phases, respectively, occur (e. g. , $BaTiO_3$, $KNbO_3$). Transitions are caused by the piling up of excessive charge on the cuboctahedral-coordinated cation due to increasing overlap of its orbitals with those of its ligands with decreasing temperature. As $BaTiO_3$ is lowered through its transition temperatures, fewer ligand orbitals become involved in σ bonding with Ba^{2+}. Since each of the O^{2-} ions is colinearly attached, the formation of short and strong σ and π bonds with one cation requires a longer and weaker σ bond with the other. The cations therefore have identical displacements in the direction of a chain. The absence or presence of π bonding perpendicular to this axis of strong interaction leads to chain alignments that are ferroelectric or antiferroelectric, respectively (compare, e. g. , ferroelectric tetragonal and orthorhombic $BaTiO_3$ with antiferroelectric tetragonal and monoclinic WO_3, respectively).

By application of group-theoretical methods, a symmetry classification of orbitals is derived for each molecular point group occurring in $BaTiO_3$. Molecular-orbital energy-level diagrams are then constructed. The number and classification of the electronic transitions can be predicted by means of the selection rules.

A comparison of a cation in acidic aqueous solution and in perovskite-type oxides reveals an astonishing similarity of bonding (e. g. , $\left[TiO(H_2O)_5\right]^{2+}$ and tetragonal $BaTiO_3$ or $\left[NbO(H_2O)_5\right]^{2+}$ and tetragonal $KNbO_3$). The cations that can form ferro- and/or antiferroelectric perovskite-type oxides must be large enough to accommodate six O^{2-} anions, and in acid solution must coordinate to one or more

27

proton-deficient oxygens (i. e. , OH^- or O^{2-}). They therefore must have low-lying, completely empty $3d \leqslant 4s, 4p$; $4d \leqslant 5s, 5p$; or $5d \leqslant 6s, 6p$ acceptor orbitals for combination with filled donor ones of O^{2-} to form strong σ and π bonds. Therefore, Al^{3+} occurring as $[Al(H_2O)_6]^{3+}$ in solution and Sn^{4+} as $Sn(H_2O)_6{}^{4+}$ are excluded from forming ferroelectrics.

Ions containing d electrons in the valence shell (e. g. , V^{4+}, Mo^{5+}, W^{5+}, Cr^{3+}) do not form ferro- or antiferroelectric perovskites, since these electrons cancel the effect of π bonds. In Na_xWO_3, $Ba_{1-x}La_xTiO_3$, and $K_{1-x}Ba_xNbO_3$, off-center distortions of W^{6+}, Ti^{4+}, and Nb^{5+} disappear with increasing x. Conductivity is of the metallic type, since the t_{2g} orbitals of the octahedral-coordinated cations must overlap sufficiently well to form a narrow conduction band.

The Model of the Distortable Double Well

While the detailed behavior of ferroelectrics seems to require a clear knowledge of specific cation-anion constellations, immersed into a crystal matrix and described by a competition of permissible molecular bonds, the essential facts of this competition can be derived through a generalized model without reference to the specific structure of the surroundings. Such models incorporating general trends have proved very useful before; e. g. , the Debye model of rotating dipoles or the Onsager model of the near field, which extracted the theory of dielectrics from the "$4\pi/3$" catastrophe, predicting ferroelectric order for all dipole molecular systems.[29]

The model of the distortable double-well proposed by us[30] took as its starting concept the fact that space for the rotation of polar groups is normally not available in crystals but that dipoles can still be inverted by flip-flop transfer between two "a priori equal" well sites. At the outset, the two positions of choice have structurally identical surroundings; inequality arises when one well site is occupied and the other empty. The surroundings react to this situation by some compensating distortion and charge-carrier motion. Thus, the filled site will deepen and the empty one flatten out as function of duration of occupation; at sufficiently low temperatures the charge carriers become immobilized by self-trapping.

The model - treated in d-c and a-c response as function of field strength, well depth, distortion-time constant, and temperature - has versatile properties: It contains the fixed equal or unequal double well as boundary cases, leads to an inherent distribution of relaxation times, and can create an anomalously large polarizability, since eventually all wells may turn with their deepened sites into

---

29) P. Debye, "Polar Molecules," Chemical Catalog Company, New York, 1929; L. Onsager, J. Am. Chem. Soc. **58**, 1486 (1936).

30) R. Fuchs and A. von Hippel, J. Chem. Phys. **34**, 2165 (1961).

one preferred direction. Thus it allows extending the discussion to ferroelectricity by identifying the wells with competing molecular bond directions and the distortion with the reaction of the crystal surroundings to the development of preferential order.

The distortable double well not only leads to a Curie-Weiss law, since well depth and distortion time can be adjusted to freeze in all charge carriers at a critical temperature T_c in the lower well site. The model also conveys a statistical picture of the nucleation and growth of dipolar order, when the distortion parameters are interpreted as direction-sensitive coupling parameters between the well sites. If two neighboring wells are occupied in identical orientation, the joint distortion makes a growth of this orientation more likely. Such direction coupling is akin to the action of a polarizing field, only here - in contrast to the long-range polarization field of the Lorentz type - a strain field is produced in the crystalline matrix. As the temperature is lowered, swarms of short-living organized regions are generated until finally the interaction between such "nuclei of order" forces on each domain the dominance of one direction because the crystal matrix requires a concerted distortion. Thus, the effect of the strain field - including polarity effects - affects the energy state of competing molecular orbitals and links long-range with short-range order.

This extension of the theory will be given elsewhere. A first application of our model has just been made to the "proton-lattice" interaction in hydrogen-bonded ferroelectric crystals by Blinc and Ribaric. [31]

Frequency Response of Ferroelectrics

Onset of the ferroelectric state lowers the crystal symmetry by development of a polar axis. This axis can be inverted and also oriented in competing equivalent crystallographic directions. Without electric or strain bias, the choice of directions is a statistical process; a domain pattern results. A sufficiently strong electric field of proper orientation can transform the crystal into a single domain by the nucleation and motion of domain walls. Coalescence of domains by alignment of their polar axes is - in general - prevented by high activation energies.

Small reversible wall motions in a-c fields produce relaxation spectra in linear response, while larger motions and domain nucleation cause nonlinear hysteresis loops. Loop saturation normally indicates an approach to single domain status with the axis pointing in the field direction. [32]

31) R. Blinc and M. Ribaric, Nuclear Institute "Josef Stefan, " Physics Department, Ljubljana, Yugoslavia, 1962. We are indebted to the authors for a preprint of their paper.

32) Cf. , however, A. von Hippel, "Molecular Science and Molecular Engineering, " The Technology Press of M. I. T. and John Wiley and Sons, New York, 1959, p. 268 for special situations.

At sufficiently high frequencies, the domain walls have no time to respond. A single-domain ferroelectric should now behave like any pyroelectric crystal; its polar axis cannot be inverted, but force and torque can be exerted on the permanent dipole system. The frequency response of this permanent moment system is the final problem at issue.

When the electric field across the crystal is uniform, the polar system responds to torque like one tremendous dipole molecule embedded in a hard but deformable medium. Turning of the dipole shears this medium and invokes a restoring torque. At a critical frequency, given by sample dimensions and elastic-wave velocity, the crystal is driven into mechanical resonance; large amplitudes make the system nonlinear, and a sequence of odd harmonics results. These are the piezoelectric resonances of ultrasound generators.

Parallel to the polar axis, the uniform field does not excite primarily such acoustical modes but superposes induced moments on the permanent moments; it acts on optical modes resonating in the infrared. Since the embedding medium is itself the dipole carrier, some cross coupling occurs between acoustic and optical mode types.

With increasing driving-field frequency a new critical situation arises, when the crystal can act as electric resonator. An electromagnetic plane wave traversing an isotropic dielectric of permittivity κ' has a wavelength

$$\lambda = \frac{c}{\nu} \frac{1}{\sqrt{\kappa'}} \quad . \tag{75}$$

This ferroelectric is an anisotropic material; also, since the ratio of light velocity to sound velocity,

$$\frac{\mathcal{V}_{opt}}{\mathcal{V}_{ac}} \approx 10^5 \, , \tag{76}$$

the sample no longer alters its shape in the electric-resonance region. It responds like a "clamped" crystal with appreciably reduced permittivity. Standing waves formed by plane waves traveling parallel to the polar axis exercise torque on the dipole system perpendicular to the polar axis and thus produce dipolar distortion modes. Standing waves formed by plane waves traveling perpendicular to the axis, on the other hand, can only induce moments by displacing the positive against the negative lattice points, hence couple into the long-wave tail of longitudinal optical wave modes. Such modes can also be excited by waves traveling parallel to the axis, but the effect is weak compared with the dipolar distortion modes, and the corresponding electromagnetic resonances occur at higher frequencies, since the dielectric constant for the distortion modes is much larger than for the inducing modes $(\kappa'_\perp \gg \kappa'_\parallel)$.

The disappearance of the ferroelectric response from microwaves to infrared can thus be clearly described: Similar to the spin waves of the ferromagnetic dipole system, dipolar distortion waves are excited in the ferroelectric dipole system (including torsion modes). For such dipolar modes of acoustic waves the name "dipolar acoustic phonons" may be appropriate. As these resonances are traversed, $\kappa_\perp$ falls systematically and reaches the nonferroelectric value given by the optical infrared vibrations when the distortion waves become so short that the kinking of the dipole system affects the magnitude of the permanent moments. When a long-range electric feedback field of the Mosotti type is active in establishing the ferroelectric state, this limit will be reached at appreciably lower frequencies than in materials where a shorter-range strain-coupling field is decisive.

If these considerations are correct, the way to excite strong ultrasound frequencies in the range from 10^9 to 10^{11} or 10^{12} cps would be to use polar-axis crystals and excite dipolar distortion modes (dipolar acoustic phonons) by resonating these crystals as electromagnetic cavities.

II.   EXPERIMENTAL APPROACHES AND RESULTS

Single-Crystal Growth by Flame Fusion

Rutile, $SrTiO_3$, and $BaTiO_3$ were chosen as the prototypes for our investigation of the basic properties of high-dielectric-constant materials; relatively large single crystals of good quality became necessary. Single crystals of TiO_2 and $SrTiO_3$ have been grown by the flame-fusion process[33, 34] and were available commercially. The latter, however, were unsatisfactory because their quality and purity varied widely and because no history of growth and annealing conditions was available. These crystals were therefore grown in the Laboratory under controlled feed-preparation and growth conditions.

Preliminary experiments on the growth of $BaTiO_3$ and $Sr_{1-x}Ba_xTiO_3$ crystals by the flame-fusion method were made. $BaTiO_3$ crystals were ultimately grown by a different method.

The flame-fusion process was invented in 1902 by Verneuil[35] for the growth of ruby ($Al_2O_3 \cdot Cr^{3+}$), and has since been used for many oxide crystals, including spinels, rutile,[33] $SrTiO_3$,[34] transition metal oxides and double oxides,[36] and rare earth oxides.[37] Of these, only Al_2O_3, spinel, rutile, and $SrTiO_3$ have been produced in commercial quantities.

33) C. H. Moore, Trans. Am. Inst. Mining Met. Engrs. 184, 194 (1949).

34) L. Merker, ibid. 202, 645 (1955).

35) A. Verneuil, Compt. rend. 135, 791 (1902).

36) E. J. Scott, J. Chem. Phys. 23, 2459 (1955).

37) L. Merker, private communication.

The flame-fusion burner (Fig. 12) is a vertical post-mix oxyhydrogen torch with flame pointing down into a ceramic muffle and impinging on a ceramic pedestal on which the crystal is grown. Provision is made for periodically introducing finely powdered oxide feed material into the center tube along with oxygen gas. The powder melts in the flame and builds up into a cone. When the latter reaches a sufficiently hot part of the flame, its tip melts and several crystallites form. The crystallite oriented in the direction of most rapid growth becomes the seed for a single crystal. Growth may also be initiated from a seed crystal attached to the pedestal.

The powder feed and flame temperature are then increased gradually and lowering of the pedestal is begun. After the crystal reaches the desired diameter, the feed, flame temperature, and lowering rate are left constant, and the crystal grows as a cylindrical boule. Crystals of the order of 1.5 cm diam. and 4.5 cm length can be grown in 3 to 5 hours. At the end of the growth period the burner is shut off and the crystal is allowed to cool to room temperature in the muffle. Because of this rapid cooling and the large temperature gradient during growth, subsequent annealing of the crystal is usually necessary to remove residual stresses.
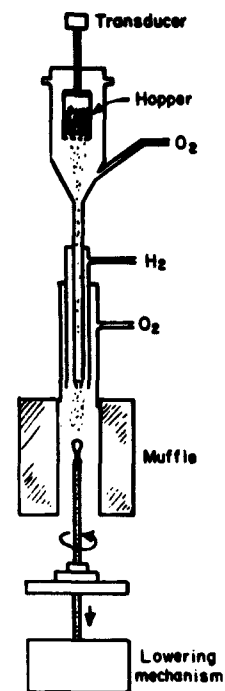

Fig. 12. Schematic of flame-fusion burner.

Preparation of Feed Material

Introduction

For the growth of consistently good-quality crystals of a particular compound by flame fusion, at least ninety percent of the effort must be expended in the preparation of a feed material of proper physical and chemical characteristics. The flame-fusion technique is essentially a single-pass floating-zone process in which material is added to the melt as discrete particles which must fuse in the flame before hitting the melt. The molten zone is so thin that solid particles impinging on it cause local supercooling with consequent surface nucleation, causing the boule to become polycrystalline. This condition can be avoided by making the particles small enough. However, too fine a particle size leads to vaporization in the flame, resulting in excessive heat loss in the flame and, particularly in the case of ternary compounds, leading to large deviations from stoichiometry in the crystal. A controlled particle-size range is necessary; it will vary from one crystal to the next, depending on such factors as vapor pressure, heat of vaporization, thermal conductivity of the material, and surface heat-transfer rates and

flame temperature gradients of the flame pattern.

An additional factor complicates matters further: The particle size that
satisfies the above conditions is usually in the submicron range, and most ma-
terials in this size range have very poor flow characteristics, tending to be
sticky or "floury" and easily forming large aggregates due to the large surface-
to-volume ratio. If such aggregates are dense, they behave as large particles.
It is necessary to form boule feed powders as large (ca. 50 μ) porous aggregates
of submicron crystallites. This can be done by precipitating a compound with a
large molecule, such as an ammonium double sulfate or oxalate, with a particle
of the desired aggregate size and then calcining the precipitate to drive off the
volatile constituents, leaving a porous aggregate of fine oxide crystallites.

While some of the physical properties described can be measured by elec-
tron microscopy, settling rates, or surface-area measurements, it is usually
simpler to test the feed in the burner by attempting to grow a crystal after a
rough evaluation in terms of "break angle" for flow, stickiness, and bulk density.

TiO_2 Feed

Since a very successful feed for the growth of Al_2O_3 crystals can be ob-
tained by decomposing ammonium alum, $AlNH_4(SO_4)_2 \cdot 12H_2O$, at $1000^\circ C$, attempts
were made to prepare rutile feed material from a double ammonium and titanium
sulfate following the procedure of Merker. [38] This was achieved by adding tita-
nium tetrachloride to a saturated chilled solution of ammonium sulfate with rapid
stirring. The double salt $(NH_6)_2 \left[TiO(SO_4)_2 \right] nH_2O$ precipitates immediately
and is recovered by filtration and washed free of HCl with saturated ammonium
sulfate solution. The value of n was determined experimentally to be approxi-
mately 6.5. After preliminary air-drying at room temperature, the double
sulfate is calcined at $900^\circ C$ for 2 hours to give a spongelike titanium dioxide with
a fluffy appearance. Material passing through a 100-mesh screen was used for
the flame-fusion process.

Feed thus prepared did not have good free-flowing characteristics; experi-
ments were therefore performed in which various experimental conditions such
as ignition temperature, acidity of the ammonium sulfate, precipitation temper-
ature and rates were altered. Rotary calcination was found to improve the feed
somewhat but the greatest improvement was obtained by making the ammonium
sulfate solution strongly acid with sulfuric acid. The resulting feed was satis-
factory without need of rotary calcination. Details of the process are given
below:

Titanium tetrachloride is dripped into a cooled solution of ammonium
sulfate in sulfuric acid to precipitate titanyl ammonium sulfate which, after

---

38) L. Merker and H. Espenschied, U.S. Patent 2,521,392 (September 5, 1960).

washing and igniting at 900°C, yields TiO_2.

The following procedure yields about 105 g of feed material after rejection of oxide held by a 100-mesh sieve: 438 cm^3 (4 mols) of $TiCl_4$ from a separating cylinder with a Teflon stopcock is dripped over a period of 4 to 5 hours into a solution consisting of 1200 g (9.08 mols) $(NH_6)_2SO_4$, 120 ml conc. H_2SO_4 and 1400 ml H_2O, the temperature being kept below 20°C and the solution agitated from below by means of a magnetic stirrer and from above with a glass stirrer.

The double sulfate is filtered under suction into a large Buchner funnel and washed with saturated ammonium sulfate solution until the washings are free of chloride (4 to 5 liters of solution usually required). The filter cake is dried on the pump overnight (filtered air being used), and is then allowed to stand in a plastic dish for 26 hours, covered with tissue to keep out dust, before ignition at 900°C for 2 hours to form TiO_2.

Attempts were made to isolate an ammonium titanyl oxalate, $(NH_4)_2$-$[TiO(C_2O_4)_2]nH_2O$, since the corresponding barium and strontium salts are used for preparing barium and strontium titanate feeds. Because of the solubility of the ammonium salt this was not accomplished; salting-out techniques produced only ammonium oxalate. Experiments in which the pH during precipitation was altered were carried out but discontinued when the sulfate process proved satisfactory.

Additions of Al, Cr, Fe, Zr, V, Nb, Ta, Mo, and W to rutile are of interest. Al, Cr, and Fe additions were attempted chemically by coprecipitation of their ammonium alums but since these alums are more soluble than $(NH_4)_2SO_4$, they could not be precipitated from solution. The mixed sulfate cannot be evaporated above room temperature because of hydrolysis of the titanium salt to $TiO_2\cdot nH_2O$. Consequently the solutions containing mixed sulfates had to be kept at room temperature until all water had evaporated. The products were gritty, cementlike materials unsuitable for boule feed. Attempts to add Fe^{3+} to the feed by adsorption were made either by dissolving $Fe_2(SO_4)_3$ with the ammonium sulfate in larger amounts than previously or by washing the precipitate of the double sulfate with ammonium sulfate containing Fe^{3+}. Again gritty feeds were obtained. Dopants were therefore added to the feeds by dry-mixing of the oxides.

The purity of the feed is of vital importance. Trace analyses by emission-spectrographic techniques were carried out on the titanyl ammonium sulfate, feed materials, and single crystals grown from the feed. The caps of the crystal were treated separately as they can be expected to contain a larger concentration of impurities due to zoning during growth.

Emission spectroscopy was chosen because chemical determinations are time consuming and no more accurate in the low range in which the impurities are usually found. A similar technique with appropriate modifications was also used in the quantitative analysis of the various doped rutile crystals. Analytical con-

ditions are listed in Table 3. Harvey's addition method[39] was used to determine the major impurities, Al, Fe, Mg, and Si. A typical analysis is shown in Table 4, which shows a high iron content. This was already suspected from the yellow color of the annealed crystal and the brown color of its "cap."

Table 3. Conditions for spectrochemical impurity
determination in rutile.

Excitation source	D-c arc
Amperage	12 amperes
Voltage	210 volts
Analytical gap	5 mm
Wavelength region	2300 to 4400 A
Exposure time	Complete arcing
Photographic plate	Eastman Kodak 1 N
Buffer	1:2, sample-to-graphite by weight
	National Carbon Co., specpure
Electrodes: Anode	Graphite, L 3803
Cathode	Graphite, L 3866

Table 4. Impurities according to Harvey's method.[39]

Element	Amount (%)
Al	0.002
Fe	0.010
Mg	0.001
Si	0.004

The removal of impurities by reprecipitation of the double sulfate was tried. According to Merker,[38] the soluble sulfate can be recrystallized by dissolving in 30% H_2SO_4 and reprecipitated by adding solid ammonium sulfate. In practice this procedure was very difficult. It was found that the sulfate was three times as soluble in 30% nitric acid than in 30% sulfuric acid, but the resulting feed no longer had satisfactory flow properties. Since reprecipitation was unsuccessful, measures were taken to cut down iron contamination in all parts of the process.

39) C. F. Harvey, "Spectrochemical Procedures," Applied Research Laboratories, Glendale, Calif., 1950, p. 218.

Teflon containers were substituted for the iron vessels received with the titanium tetrachloride from Titanium Metals Corporation, resulting in lighter color. A Globar furnace built with alumina bricks was used for calcination of the double sulfate.and a titanium shovel for transfer of the hot ignition trays. The air passing through the filter cake before ignition was passed through an ultra filter to remove air-borne dust particles. Micron filters were placed in the gas lines of the Verneuil burners and the burner assembly stripped down and made iron-free.

Despite these precautions the crystals contained 20 to 100 ppm iron, leading to the conclusion that it came from the titanium tetrachloride. No satisfactory source for high-purity $TiCl_4$ has been found; a simple distillation procedure[40] was therefore used. Significant improvement in the transition element content of the feed was noted by spectrochemical analysis, but a considerable amount of silica was picked up from the glass column. Further work on distillation and zone-freezing techniques is in progress.

A feed powder, satisfactory as regards the physical properties, was thus obtained but its chemical purity remains a problem.

Barium and Strontium Titanate Feeds

Double oxalates of some alkali earth metals with titanium, e. g., $Ba\left[TiO(C_2O_4)_2\right] \cdot 4H_2O$, yield a stoichiometric titanate on ignition. Aqueous titanium tetrachloride solution is mixed with an almost twofold excess of oxalic acid at 70^oC, producing an acid solution of titanyl oxalate. To this is added a hot solution of barium or strontium chloride in an amount equivalent to the titanium. In the case of barium, immediate precipitation takes place, but with strontium from dilute solutions precipitation is slow. The precipitate is stirred for four hours, filtered, and washed free of chloride with demineralized water. The precipitate is then calcined at 1000^oC for two hours. For the preparation of a suitable strontium titanate feed, dilute solutions had to be used,[34] and material between 100 and 270 mesh resulted in the best single crystals. It is desirable, especially with barium titanate, to produce a dry precipitate before ignition because a damp filter cake produces gritty feed. Barium titanate prepared by the above method was also used for crystal growth from the melt. Details of both processes are given below.

Barium Titanate

An aqueous solution of titanium tetrachloride, prepared by dripping 165 ml (1. 50 mols) of $TiCl_4$ into 500 ml of water below 20^oC, is added to a solution of oxalic acid, 630 g (5.00 mols) $(COOH)_2 \cdot 2H_2O$ in 1320 ml of water and kept at 20^oC.

40) W.S. Clabaugh, R. T. Leslie, and R. Gilchrist, J. Research Natl. Bur. Standards 55, 261 (1955).

To this mixture is added, with rapid stirring from top to bottom, a solution of barium chloride at $70^{\circ}C$, 391 g (1.60 mols) $BaCl_2 \cdot 2H_2O$ dissolved in 900 ml H_2O. The barium titanyl oxalate after $4\frac{1}{2}$ to 5 hours of agitation is filtered under suction and washed free of chloride with distilled water (8 to 12 liters). The filter cake is then dried by suction overnight and gives a powdery product which, after ignition at $1000^{\circ}C$ for 2 hours, yields almost the theoretical amount (350 g) of $BaTiO_3$.

Strontium Titanate

Here the method is similar. Forty ml (0.363 mols) of $TiCl_4$ is dissolved in 121 ml H_2O and is added to a solution of 177 g (1.40 mols) of oxalic acid at $70^{\circ}C$. To this is added 152 g (0.570 mols) $SrCl_2 \cdot 6H_2O$ in 590 ml H_2O at $70^{\circ}C$. The procedure is then the same as for $BaTiO_3$.

Mixed Titanate Feed

Mixed barium strontium titanates, $Sr_{1-x}Ba_x$, TiO_3 have been made. The feeds, made similarly to those of the individual titanates, were of a very fine particle size. In order to coarsen the particles, the double oxalate, (BaSr) $\left[TiO(C_2O_4)_2 \right] nH_2O$, was precipitated slowly, the alkaline earth chloride solution (at $70^{\circ}C$) being dripped into the titanyl oxalate solution. This did improve particle-size distribution somewhat, although the portion between 200 and 270 mesh is still very small. However, much more is held by a 400-mesh sieve. The growth of crystals from this feed is yet to be attempted.

Burner Design

The design of flame-fusion research equipment may be divided into several parts: a stable supply of oxygen and hydrogen gases, a rigid, vibration-free mounting for the burner, the torch, feed hopper, and crystal-lowering mechanism.

The oxygen-distribution system is shown in Fig. 13. The hydrogen system is similar but also has a hydraulic flashback arrestor at the manifold. The gases are brought into the burner room in 1-inch welded iron pipe as far as the station valves. From there, $\frac{1}{4}$-inch copper tubing is used for all burner lines. Each burner uses up to 40 cfh of hydrogen and smaller amounts of oxygen; duplex five-tank manifolds were therefore used for the three burners set up.

The regulation system, including the large-diameter supply piping, insures that pressure fluctuations from manifold switching and burner flow adjustments cause no observable fluctuations in the burner gas flows. Simultaneous shut-off valves are a necessary safety precaution, and also insure that the delicate metering valves are not used for shut-off purposes.

The burner, consisting of the feed hopper, torch, muffle, and crystal-lowering mechanism, is shown in Fig. 14. The parts are mounted on a drill-press stand attached to I beams on the wall in such a manner that it can be plumbed. The
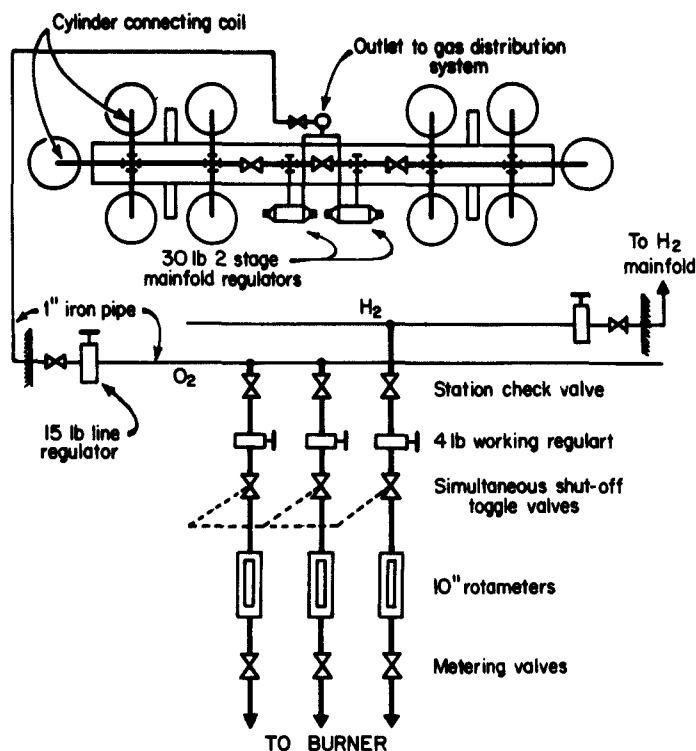
37

Fig. 13.

Gas-distribution
system.

various parts are mounted on standard drill-press fixtures or collars, allowing vertical adjustment of all components.

The crystal-lowering mechanism is shown in Fig. 15. The main design requirements were structural rigidity, rapid and smooth manual lowering, and adjustable-speed automatic lowering. Originally rotation of the crystal support was possible, but this feature was abandoned when it was found to give no improvement in crystal growth.

The crystal is grown on a $\frac{1}{2}$-inch diam. by 8 to 12 inches-long stabilized zirconia pedestal supported in a simple flat-base steel holder. The holder stands on a circular platform supported by a large-diameter brass column attached to the lowering carriage. This arrangement permits easy centering of the pedestal in the burner flame. The carriage rides on two steel columns and the height can be adjusted with a 10-pitch lead screw. Rapid manual adjustment is obtained with a hand wheel attached directly to the bottom of the lead screw, and automatic traverse by a swing-in worm gear connected to a variable-speed motor. The attachment of the mechanism to the drill-press column permits shimming, so that the carriage traverse can be made vertically plumb.

The torch design finally used is a modification of a standard Verneuil burner used in commercial production of rubies and spinels.[41] It is a three-tube coaxial-

41) L. Merker, FIAT Final Report No. 1001, 1947.
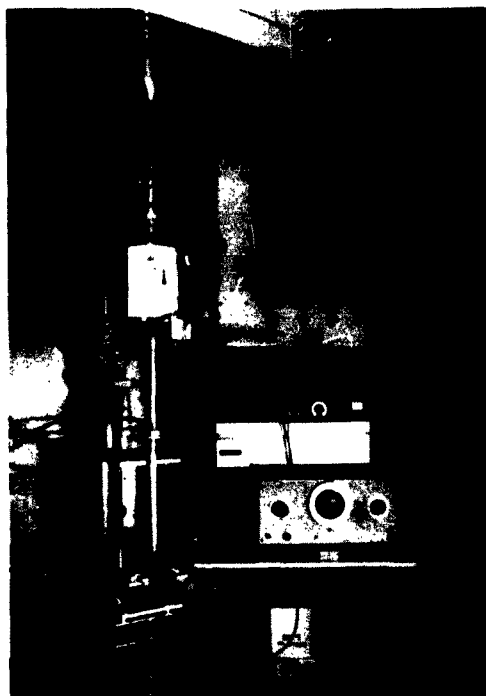
Fig. 14. Flame-fusion burner.   Fig. 15. Crystal-lowering mechanism.

type post-mix burner, but avoids the sharp turbulent mixing zone of the usual tri-
cone torch. [33] The torch, with tips suitable for growth of TiO_2 and $SrTiO_3$, is
shown in Fig. 16. It is air-cooled and constructed entirely of brass for ease of
machining and avoidance of transition metal ion contamination. Materials with
melting points from 1500° to 2450°C have been grown with this type of torch, with
variations in center and intermediate tip diameters and recessions.

The torch is supported at the top by the powder hopper and positioned by a
three-point support around the outer sleeve to permit the unit to be plumbed.
Plumbing the burner accurately is vital for successful operation and is accomplished
with a plumb line through the central tube.

The outer tip of the torch is recessed into a cast alumina or zircon muffle.
The muffle design used is shown in Fig. 17. The i.d. varies from $1\frac{1}{2}$ to 2 inches.

The largest source of difficulty in applying the flame-fusion technique to the
growth of a wide variety of crystals stems from the necessity of handling feed
powders with a large diversity of flow characteristics. In most flame-fusion equip-
ment, mechanically or electrically (solenoid) operated hammers are used to tap
screen-bottomed hoppers in order to produce powder flow. These simple systems
place severe limitations on the flow and packing properties of the feed powder, and

39
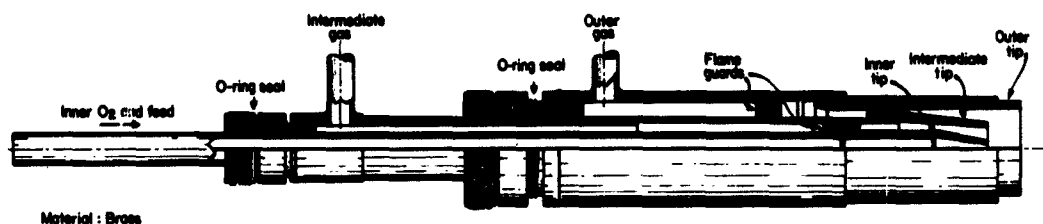
Fig. 16. Three-tube flame-fusion torch.
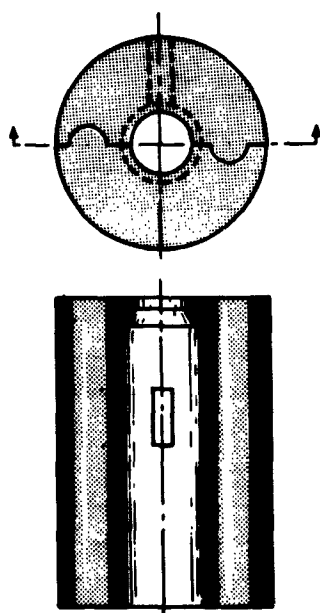
Fig. 17. Muffle design.
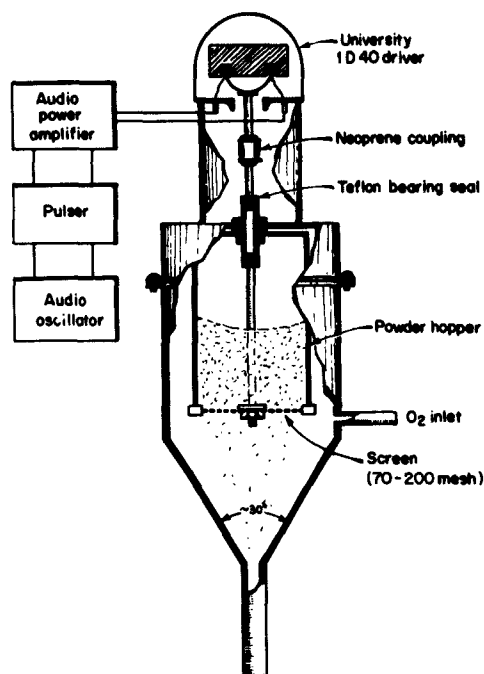
Fig. 18. Burner-feed system.

necessitate considerable chemical feed development work on the physical character-
istics of the powder before satisfactory or, indeed, any crystals can be grown.

A more complex but also more versatile powder feed system has been de-
veloped at this laboratory (Fig. 18). The hammer is replaced by a loudspeaker,
usually a high-power driver, whose diaphragm is coupled directly to a screen at
the bottom of the powder hopper by an aluminum rod. The rubber coupling protects
the diaphragm and corrects any small bearing misalignment. The loudspeaker is
driven by an audio power amplifier excited by an audio oscillator operated through
a circuit which supplies gating pulses of independently controlled duration and fre-
quency. The audio frequency and power of the pulse are controlled at the oscillator.

The flexibility of the control system allows powders of varying physical

characteristics to be dispensed at a controlled rate, even through very fine
screens, with little undesired variation. The variable audio-frequency also
permits tuning to a near-resonance condition of the gas column in the inner burner
tube, thus inhibiting the tendency of many feed powders to stick to the walls.

Two of these units have been in constant use for several months and have
proven very satisfactory for the growth of ruby, rutile, titanates, and various
transition metal oxides.

Crystal Growth

A large part of the development work in growing a given crystal by flame
fusion involves the preparation of a suitable feed material. If a good feed material
is available, determination of the proper growth parameters is relatively straight-
forward, although time-consuming. In the case of rutile, feed was available[*] and
little difficulty was encountered in crystal growth. The major effort here was in
producing a purer feed. This effort was not completely sucessful, and work is
continuing on it.

For $SrTiO_3$ crystals, no feed material could be purchased, and development
of the growth techniques and feed-material preparation had to proceed together.
Details of a successful feed-preparation technique are given on pp. 36 ff. Growth
techniques for both crystals are described below, together with data on preliminary
experiments on the growth of $BaTiO_3$ and $Ba_xSr_{1-x}TiO_3$.

Rutile

Rutile crystals were grown in the three-tube coaxial burner, the gases,
from the center outward, being oxygen, hydrogen, and oxygen, insuring relatively
oxidizing atmosphere. The center and intermediate tips of the burner are tapered
and measure 1/8 inch and 11/16 inch i.d., respectively, at the tapered ends. The
outer tip is straight and measures $1\frac{1}{4}$ inches i.d.

The center and intermediate tube tips are both recessed $\frac{1}{2}$ inch into the outer
tube tip, thus providing the optimum temperature distribution with regard to both
radial and vertical thermal gradients. This arrangement provides a high-temper-
ature region extending radially for about 3/4 inch to 1.0 inch at a position about
4.0 inches below the tips.

To a large extent the gradients are modified by the growing crystal. The
optimal crystal-growth conditions occur when the crystal has reached its maximum
width ($\sim 3/4$ inch). The hot zone then completely envelops the cap of the crystal,
insuring fairly even temperature and feed distribution, with a sharp vertical
thermal gradient. Both gradients are affected by the inner diameter and composi-

---

[*] Courtesy of Dr. M. D. Beals, Titanium Division, National Lead Company,
South Amboy, N.J.

tion of the muffle. The best diameter is 2.0 inches in either cast alumina or zircon. The gas flows for rutile are standard for our burners and do not require much modification when doping agents up to 1.0 or 2.0% are added.

The outer oxygen tube is maintained at a constant flow of 14 liters/min. The oxygen flow in the center tube is kept nearly constant at 4 to 4.5 liters/min. The hydrogen flow in the intermediate tube is varied from 10, at the start of crystal growth, to about 20 liters/min. at its termination.

The feed powder is sieved before use and the < 100-mesh fraction used for growth. A 70- or 80-mesh screen is used in the feed hopper and vibrated 35 to 40 times per minute.

Rutile crystals have been grown from seeds and from sintered cones. The former are usually oriented on the c or a axis. Rutile may evidently be grown with equal facility in any direction when seeded. However, the preferred growth direction noted in crystals grown from sintered cones is along the c axis.

The crystals are annealed embedded in TiO_2 boule feed in a stabilized zirconia crucible for 24 hours at 1100° and cooled at $25^\circ C$/hr. Further oxidation at 600° to $800^\circ C$ may be required. Boules weighing 15 to 25 g and up to 1.5 cm diam. by 3 to 4 cm length were produced.

$SrTiO_3$

$SrTiO_3$ crystals were grown using the three-tube coaxial burner with oxygen, oxygen, and hydrogen in the center, intermediate, and outer tubes, respectively. This gives the higher-temperature reducing flame required to maintain the boule cap at $2050^\circ C$, the melting temperature of $SrTiO_3$. The temperature is increased by varying both center and intermediate oxygen flows.

$SrTiO_3$ crystals are quite sensitive to small changes in thermal conditions; consequently it is necessary to control the flow rates of gas and feed very carefully. A muffle of cast alumina having an inside diameter of $1\frac{1}{2}$ to $1\frac{3}{4}$ inches is optimum. The feed is sieved before use and the - 200 + 270-mesh fraction used for growth (50 to 75 micron aggregate size). All other fractions are either discarded or retained for use in annealing the crystal. About 2% SrO is added to the feed to compensate for the SrO lost from the crystal in the flame. The size of the tips and their recession in the outer tip are the same as for rutile.

The hydrogen flow in the outer tip is kept constant at 27 liters/min., while both the center and middle oxygens are variable. Typical initial oxygen flows are: center 3 liters/min. and intermediate 2 liters/min., while the flows at the termination of crystal growth are: center 5 liters/min. and intermediate 4 liters/min.

The feed mechanism must also be well controlled and a sieve of 140 mesh (105 microns) is used in the hopper. This sieve is vibrated about 35 times per minute.

The crystals can be seeded but this requires considerable care. Crystals grown from a sintered cone are quite satisfactory; these most commonly grow in the $[110]$ direction. Doping is feasible, and Co^{3+}-doped $SrTiO_3$ crystals have been grown with up to 1% by wt. of Co^{3+} without large changes in the procedure.

The crystals are annealed embedded in $SrTiO_3$ feed material in stabilized zirconia crucibles for 24 hrs. at 1350°C and cooled at 25°C/hr. Further oxidation is usually unnecessary.
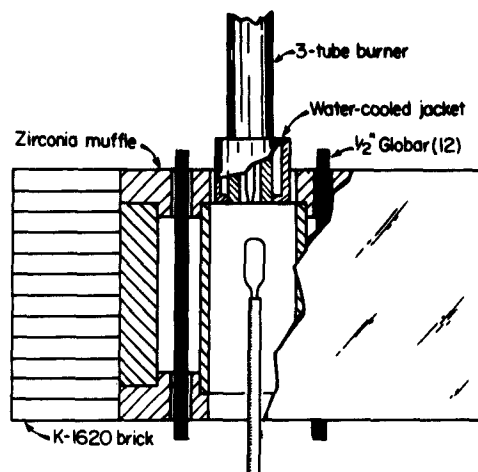
Fig. 19. Flame-fusion annealiing furnace.

$BaTiO_3$

It has been reported[33] that $BaTiO_3$ can be grown by flame fusion. This was attempted, and small crystals were obtained of both the pure material and of $BaTiO_3$ doped with varying amounts of Ca or Sr to obtain the desired ferroelectric phase. Various burner configurations were tried, but all crystals emerged badly cracked and exhibited very complex domain patterns, indicative of severe strain. In an effort to reduce the strain by reducing the temperature gradients during growth, the externally heated muffle of Fig. 19 was designed. Since the melting point of $BaTiO_3$ is only 1630°C, Globars were used as heaters. With this muffle, wall temperatures of the order of 1550°C could be maintained during growth, dropping to 1400°C on shut-off. The muffle was then slowly cooled to room temperature at a controlled rate.

No significant improvement in crystal quality was obtained and it was concluded that a major effort would be necessary to improve the quality of the feed material. It appeared that better crystals could be grown by another method (see p. 46), therefore no further work was done on this material by flame fusion.

Mixed Titanates

Since $SrTiO_3$ was grown successfully by flame fusion, some experiments were directed toward seeing if small additions of $BaTiO_3$ could be added to obtain $Sr_{1-x}Ba_xTiO_3$ $(0.1 < x < 0)$. No success was obtained with dry, mixed feeds, obtained either by mixing the titanates or by mixing the oxalates and cocalcining. Some fractured boules were obtained when coprecipitated feeds were used, but most were cloudy because of poor feed stoichiometry. Further work on feed preparation will be necessary before such crystals can be grown.

Growth of Butterfly-Wing Crystals

Good-quality, undoped butterfly-wing crystals were required for frequency-response measurements in the infrared through the millimeter spectral regions. Based on the Remeika process[42] for growing triangular crystals of BaTiO$_3$ from a KF melt, a Globar melt furnace with programmed temperature control was set up and some of the parameters affecting the growth were investigated.

Previous work[43] indicated that the particle size of the BaTiO$_3$ powder should be < 1 μ; boule feed powder made by the oxalate process was therefore used. A mixture of 10/90 mole % BaTiO$_3$/KF was placed in a 200-ml Pt crucible for all experiments. The covered crucible was placed in a furnace at the soak temperature, held for 12 hours, cooled at 25°C/hr. to the pouring temperature; here the flux was poured off and the crystals annealed down to room temperature. The effects of various soak temperatures and pouring temperatures on the size and thickness of the butterfly-wing plates are shown in Figs. 20 and 21. Higher
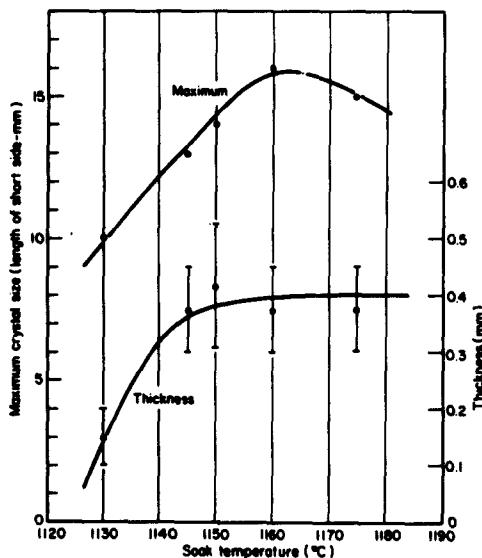
Fig. 20. Butterfly-wing size as function of soak temperature.
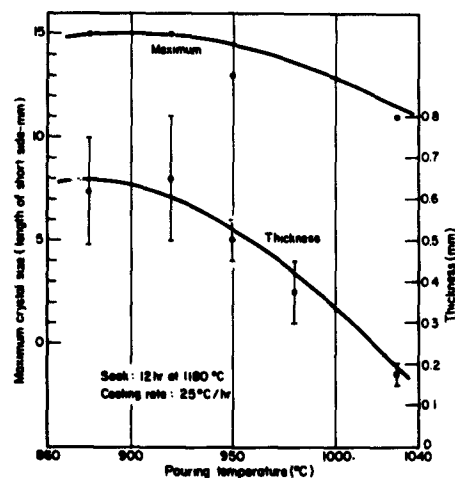
Fig. 21. Butterfly-wing size as function of pouring temperature.

soak temperatures and lower pouring temperatures yielded larger, thicker, and less perfect crystals which were dark brown instead of the greenish-blue color of the thinner plates. Optical absorption spectra of the two types are shown in Fig. 22.

42) J. P. Remeika, J. Am. Chem. Soc. 76, 940 (1954).

43) J. W. Nielsen, R. C. Linares, and S. E. Koonce, J. Am. Ceram. Soc. 45, 12 (1962).
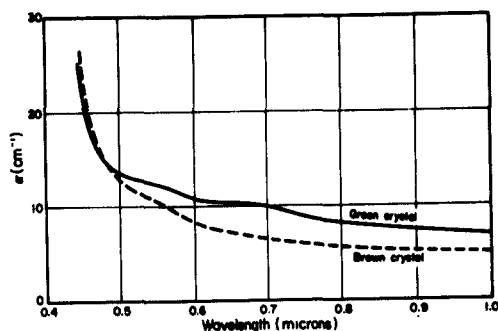
Fig. 22.

Optical absorption of $BaTiO_3$ butterfly-wing crystals.

In order to put more $BaTiO_3$ into solution at lower soak temperatures and to decrease concentration gradients prior to growth, some batches were stirred with a Pt stirrer during the soak period. While lower soak temperatures could be used, they brought about no improvement in crystal size or quality. Attempts were also made to decrease nucleation by partially covering the undissolved $BaTiO_3$ cake with perforated Pt foil at the end of the soak period. Again no improvement in crystal size or quality resulted.

The crystals are contaminated with 100 to 1000 ppm Pt, 500 to 1000 ppm F, and > 100 ppm K. These crystals were grown on a routine basis, as needed.

Growth by Pulling Techniques

The butterfly-wing crystals described proved quite unsuitable for breakdown measurements. The large amount of fluorine contamination leads to high values of conductivity; the limited thickness available is also a disadvantage. Some success has been obtained by other workers in growing $BaTiO_3$ from the melt by the flame-fusion,[44] Stockbarger,[45] and pulling[46] techniques, but their crystals were badly strained,and in most cases either Sr or Ca had to be added in order to obtain the ferroelectric form.

The suitability of three fluxed melts for pulling sizeable boules of pure $BaTiO_3$ at a temperature below the hexagonal-cubic transition was investigated. The Globar furnace used for butterfly-wing growth was modified by the addition of a pulling mechanism and provision for viewing the melt as shown in Fig. 23.

$BaTiO_3$-KF was studied first. No sucess was obtained in pulling attempts, although one small cube (~ 5 mm on edge) grew on a seed suspended below the

44) L. E. Lynd and L. Merker, U.S. Patent 2,723,916 (Nov. 15, 1955).

45) J. Smiltens, Progress Report No. X, Lab. Ins. Res., Mass. Inst. Tech., Nov., 1951, p. 27.

46) F. H. Horn, J. Appl. Phys. 33, 1615 (1962).

45
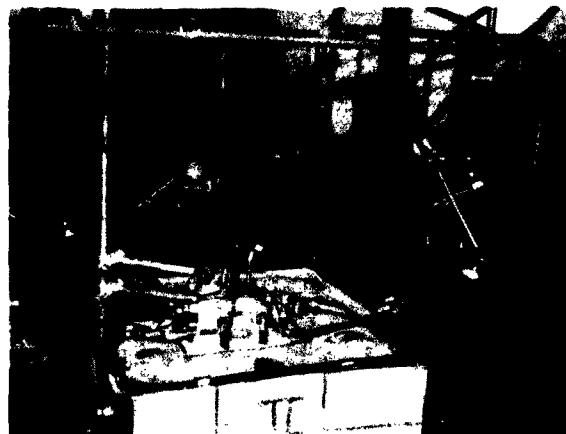
Fig. 23.

Crystal-pulling furnace.
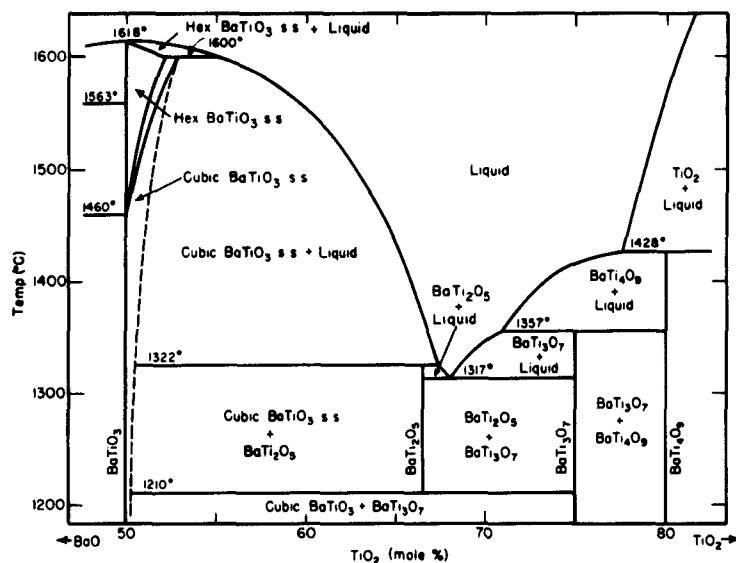
Fig. 24.   Enlarged portion of the phase-equilibrium diagram of BaO-TiO$_2$
(s. s. = solid solution).   (After Rase and Roy.[48])

surface of the melt.   Vaporization of the KF was quite troublesome in this system.

The BaCl$_2$-BaTiO$_3$ system[47] appeared more suitable, because vaporization
of BaCl$_2$ should be less of a problem, and K would be eliminated as an impurity.
Still, only small blade crystals were obtained, with some evidence of attack on the
crucible.   Growth was very slow.

A third system investigated was BaTiO$_3$-TiO$_2$.   Its phase diagram (Fig. 24)
has been given by Rase and Roy. [48]   This system has the advantage that no foreign

47)   D. E. Rase and R. Roy, J. Phys. Chem. 61, 746 (1957).
48)   D. E. Rase and R. Roy, J. Am. Ceram. Soc. 38, 110 (1955).

46

ions are present, although it is claimed that 1 to 2 mole % excess of TiO_2 should be included in the crystal. The melt used consisted of 67/33 mole % TiO_2/BaO, with a liquidus temperature of $\sim 1390^\circ C$. Single crystals of $BaTiO_3$ up to 2 cm diam. by 1 cm long have been grown (Fig. 25).

Figure 26 shows a detailed schematic of the crystal-growth furnace. The temperature is controlled by a thermocouple in the Globar chamber, while the melt temperature is determined by a Pt/Pt 10% Rh thermocouple immersed in the melt. Unlike Horn,[46] we have observed no appreciable attack by molten $BaTiO_3$ on either the thermocouple or the platinum crucible.

Fig. 25. $BaTiO_3$ crystal grown by the pulling method.

A typical growth procedure consists of soaking the melt overnight at ca. $1420^\circ C$, lowering the melt temperature to $\sim 1396^\circ$ and immersing the seed about 1 mm with 3000 sccm air flow through the seed rod. The seed is allowed to "melt in" for 30 min. , then the melt is cooled at $5^\circ C/hr$. for 1 hour. Pulling is then started at 0. 25 mm/hr. and the cooling rate set at 2 to $3^\circ C/hr$. The seed rod is rotated at 60 rpm and reversed at 30-sec intervals. The crystal is pulled from the melt at $1335^\circ C$ and annealed slowly to room temperature.

Pronounced face development was observed on these crystals and a study of these forms was made in order to determine the most desirable growth direction. The faces of the crystals were indexed by means of interfacial angles measured with a contact goniometer. Questionable crystal directions or faces were identified with back-reflection Laue X-ray patterns.

Three crystallographic directions were used for seeding: [110], [100], and [111].* The results of experiments with these oriented seeds have shown that [110] is the direction of preferred growth and that crystals grown from this orientation are large and symmetrical.

Seeds oriented parallel to [100] have produced single crystals, but these are not as large or as symmetrical as those grown from [110] seeds, while orientation of seeds parallel to [111] gives polycrystalline masses.

The forms which developed on the fully grown crystal (2 to 3 cm diam.) are {210} , {100} , {111} and rarely {110} . These forms are illustrated in Fig. 27.

---
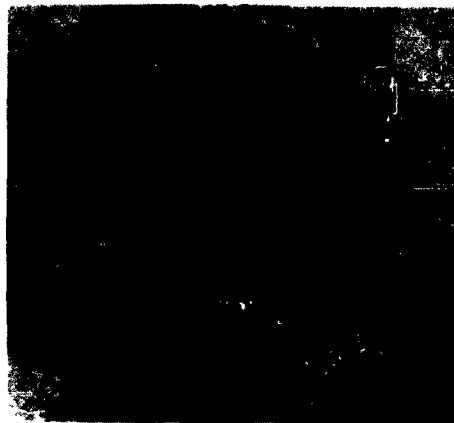
* The symbol [ ] indicates a direction in the crystal; ( ) indicates a specific face, and { } a form which is a number of faces of the same kind related by symmetry.

A) BaTiO₃ seed
B) BaTiO₃ + TiO₂ melt
C) Pt crucible
D) Zirconia crucible
E) Zirconia brick posts
F) Closing brick
G) K-30 fire brick

Motor

Water in

Air in

Water out

Motor

Light source

Air out

Mirror

Mirror

Lava plug

Quartz window

TC

Telescope viewer

F

TC control

C

A

B

Globar heater, 1 of 8
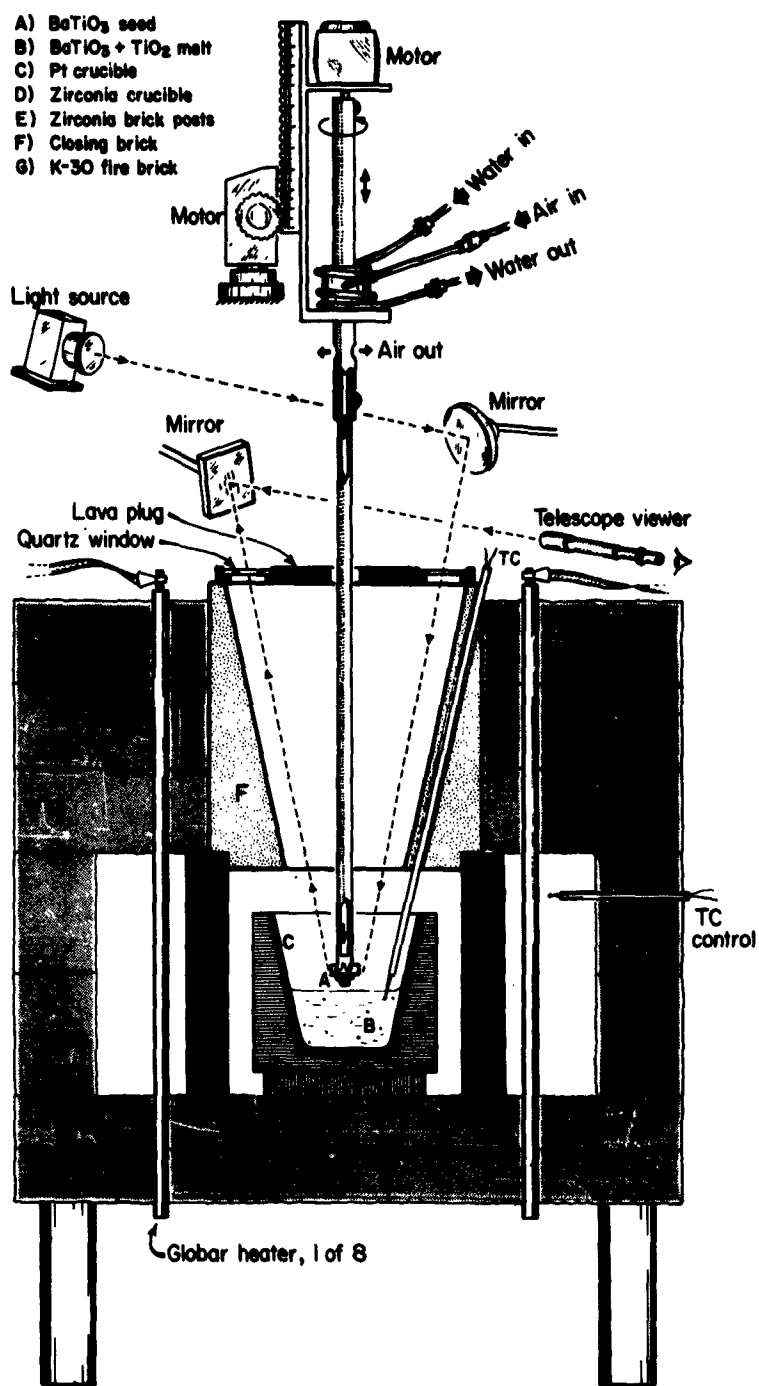
Fig. 26. Schematic of crystal-pulling furnace.

The $\{210\}$ forms are always well developed and are often the largest faces. They seem to occur because the $\{110\}$ grows out rapidly, leaving the $\{210\}$ as steps for further growth.

The $\{111\}$ forms which are large and well represented also appear to originate because of the rapid growth of $\{110\}$. DeVries[49] has noted that $\{111\}$ is a common form on small BaTiO$_3$ crystals (0.5 to 2.0 mm); this agrees with our observations. Hence $\{111\}$ would appear to be one of the first modifications to evolve. Our crystals also display re-entrants which are reminiscent of twinning in certain forms of BaTiO$_3$ "butterfly wings."

Fig. 27. Form development of barium titanate single crystal, showing faces and re-entrants. The growth direction [111] is perpendicular to the plane of the illustration. (R indicates the occurrence of the re-entrants.)

Actually these re-entrants are the result of alternating (210) and (120) faces (cf. Fig. 27 at R), which occur as steps in place of (110) faces. They commonly occur on crystals grown from [110] seeds.

Observations on our small crystals (< 5 mm in diameter) reveal the following forms: $\{100\}$, $\{111\}$, $\{110\}$, and $\{210\}$. $\{100\}$ and $\{111\}$ are the best developed while $\{110\}$ is small but evident. $\{210\}$ forms occur as modifications of $\{110\}$ even at this size; the re-entrants are also present. Ideally, BaTiO$_3$ single crystals probably evolve from dodecahedrons which add $\{111\}$, $\{100\}$, and finally $\{210\}$ forms.

Table 5. Impurities in various BaTiO$_3$ crystals.

Impurity elements (% by weight)									
Sample No.	Al	Fe	Mg	Mn	Pb	Si	Pt	K	F
1	0.003	0.01	0.001	0.001	0.001	0.03	ND	ND	ND
2	0.001	0.005	0.005	0.0005	0.0005	0.01	0.04	0.01	0.3
3	0.001	0.004	0.0006	0.0005	0.0006	0.02	ND	ND	ND

ND - not detected.

No. 1 - BaTiO$_3$ powder; No. 2 - butterfly-wing grown with sample No. 1 and KF; No. 3 - pulled crystal grown with Sample No. 1 and TiO$_2$.

49) R.C. DeVries, J. Am. Ceram. Soc. 42, 547 (1959).

The purity of these crystals is much better than that of the butterfly wings. An analysis of the two types together with the feed material is shown in Table 5. The main impurities in the pulled crystals are Fe and Si from the $TiCl_4$ feed stock.

Precise electrical measurements of the properties of the pulled crystals have been delayed by the difficulty of poling these large bulk crystals. However, a Curie point of 129.5°C, identical to that of high-purity $BaTiO_3$ ceramic, has been measured. The X-ray pattern agrees with the NBS standard, but more precise measurements will have to be made to see if any excess TiO_2 is incorporated in the lattice. Chemical analyses indicate that the compound is stoichiometric within $\pm 0.1\%$.

Evaluation work on these crystals is continuing.

Preparation of Alkaline Earth Titanate(IV) Compounds from Esters

Barium titanate(IV) may be prepared from aqueous solution.[50] Upon addition of a titanium ester (such as tetraisopropyl titanate[*]) to an aqueous solution of a barium salt, at pH 11 to 14, crystalline $BaTiO_3$ is precipitated. Flaschen used potassium hydroxide to control the pH.

In our preparation of $BaTiO_3$,[51] a 0.25 molar (0.5 normal) concentration of $Ba(OH)_2$ replaces the KOH solution in Flaschen's procedure to avoid K^+ ions in the reaction. A sufficient excess of $Ba(OH)_2$ results in a final $Ba(OH)_2/Ti(OR)_4$ mole ratio $>1/1$, thus assuring that the pH of the solution remains > 12.

Strontium titanate(IV) can be prepared in the same way by substituting a 0.25 M solution of $Sr(OH)_2$ for $Ba(OH)_2$. Extension of the method to calcium titanate(IV), however, is not possible by simple substitution of $Ca(OH)_2$ for $Ba(OH)_2$, because a saturated solution of $Ca(OH)_2$ has at 25°C a concentration of only 0.02 M and even less at higher temperature.

Calcium hydroxide combines with cane sugar, forming saccharates, and therefore dissolves much more readily in sugar solutions than in pure water; e.g., a solution containing 12% sucrose or glucose easily dissolves CaO to give a concentration of 0.25 M $Ca(OH)_2$. When this solution was tried, the only reaction obtained was hydrolysis of $Ti(OR)_4$ (R = $-CH\begin{smallmatrix}CH_3\\CH_3\end{smallmatrix}$) to $TiO_2 \cdot nH_2O$, because Ca^{2+} is strongly complexed with sugar. If a chelated titanate such as triethanolamine titanate is used, which is much less susceptible to hydrolysis, no reaction with the calcium hydroxide saccharate takes place.

Calcium titanate(IV) may be prepared by the slow addition of a calcium salt, such as $Ca(NO_3)_2$, to an aqueous solution of a strong organic base, e.g., the quaternary ammonium hydroxide $[(C_2H_5)_4N]OH$, and a chelated titanate, e.g.,

50) S.S. Flaschen, J. Am. Chem. Soc. 77, 6194 (1955).

* Provided by E.I. du Pont de Nemours and Co.

51) Progress Report No. XXVIII, Lab. Ins. Res., Mass. Inst. Tech., Jan., 1961, p. 16.

triethanolamine titanate. The ammonium hydroxide ionizes completely in aqueous solution, and hence has the same basic strength in water as NaOH or KOH. The Ca^{2+} ion concentration becomes independent of the hydroxide ion concentration, provided the solubility product of $Ca(OH)_2$ is not exceeded. Since the pH now depends upon the concentration of $[(C_2H_5)_4N]OH$ and not of $Ca(OH)_2$, the medium may have the alkalinity required for the formation of $CaTiO_3$. The chelated triethanolamine titanate is stable in basic solution except in the presence of alkaline earth ion. In the presence of Ca^{2+}, Sr^{2+}, or Ba^{2+}, $CaTiO_3$, $SrTiO_3$, or $BaTiO_3$ respectively is formed. This procedure[52] also eliminates the possible presence of K^+ of the Flaschen method. A mechanism for these acid-base reactions has been previously discussed.[53]

The behavior of a cubic modification of colloidal particles of $BaTiO_3$ obtained in aqueous solution was studied by differential thermal analysis, X-ray diffraction, density measurements, and electron microscopy. The low-density metatitanate in a loose state of crystallization was found to undergo a series of transitions with rising temperature until it reached the stable tetragonal form with normal lattice constant. The material yielded ceramics with a broadened Curie region (Fig. 28).
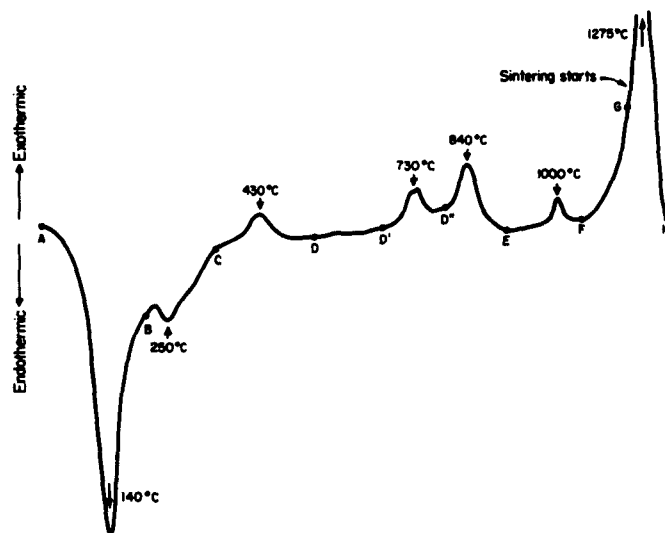
Fig. 28. DTA curve of colloidal BaTiO₃ in covered high-density alumina sample holder and static air.

52) Prog. Rep. No. XXX, Lab. Ins. Res., Mass. Inst. Tech., Jan., 1962, p. 7.
53) Ibid, p. 66.

Problems of Small Batch Preparation

An ideal ceramic for the study of the interactions between molecular structure and electrical properties would have: uniform chemical composition of high purity; single-crystal density with no voids greater than unit-cell dimensions; completely random orientation of crystallites, isotropic; freedom from strains; and uniform grain size. These goals are obviously incompatible. In practice, plastic or viscous flow and/or grain growth must be used to achieve high density because the starting powders are always poorly packed with voids occupying 20 to 40 percent of the volume. In preparing mixed ceramics it is always tempting to mix powders of the two components physically and depend on thermal diffusion during hot sintering to complete the chemical mixing. This procedure has worked well for the (Ca-Ba)TiO$_3$ and (Ca-Sr)TiO$_3$ series as judged by the regular change in dielectric properties with composition (cf. p. 67). The (Ba-Sr)TiO$_3$ series and mixtures of BaTiO$_3$ and LaAlO$_3$ have yielded poor results despite repeated crushing and remixing. Chemical mixing is certainly preferred but requires much time and labor.

For the beginning of our attempt to determine the best forming processes we have avoided the mixing problem and prepared samples from powders having the final chemical composition. Measurements of density, grain size, and electrical properties were used to compare various procedures and to judge uniformity.

Forming Methods and Equipment

For preforming, samples were dry-pressed to a thickness of 1 to 3 mm, diameter 5 to 10 mm, with unidimensional pressures between 10,000 to 20,000 psi. For final forming, hot-sintering, melting, hot-pressing, and further cold-pressing methods were investigated.

Hot-sintering was done either slowly in conventional Globar furnaces or rapidly in a special resistance-strip furnace. The latter was of a type used previously for melting-point determinations[54, 55] and for the study of phase diagrams.[56, 57] The principal features of this water-cooled metal container with adjustable copper electrodes are shown in Fig. 29. The heater elements, cylinders $2 \times \frac{1}{2} \times 0.005$ inch, are fed from a variable 4-volt, 500-amp. transformer supply.

54) H. v. Wartenberg, Handbuch der Experimentalphysik, Vol. 9, Akademische Verlagsgesellschaft, Leipzig, 1929, p. 1.

55) C. Müller, Handbuch der Physik, Vol. 21, Springer, Berlin, 1926, p. 370.

56) G. K. Burgess, J. Research Natl. Bur. Standards 205, 242 (1920), Sci. Paper No. 198.

57) W. O. Statton, Tech. Rep. 31, Lab. Ins. Res., Mass. Inst. Tech., April, 1950.
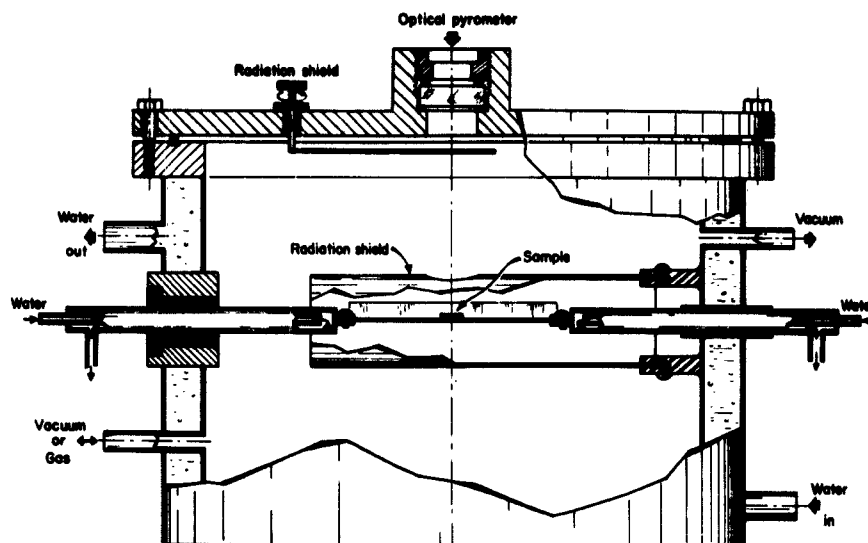
Fig. 29. Resistance-strip furnace.

Table 6. Heater-element metals for resistance-strip furnace.

Heater-element metals	Maximum working temperature	Atmosphere	Pressure
Molybdenum	2200°C	N_2, H_2 Vacuum	1 atm ~1 μ
Tungsten	2500°C	N_2, H_2 Vacuum	1 atm ~1 μ
Platinum	1550°C	Air, oxygen	1 to 10 atm
80% Platinum 20% Rhodium	1750°C	Air	1 atm
Iridium	~2000°C	Air (limited to short time)	1 atm

Radiation shielding was sometimes added to the heater by using copper supporting bolts to the wall. Temperature ranges for various heater materials are listed in Table 6. Optical pyrometer readings of temperature through the Vycor glass window were corrected for emissivity[58] and for the influence of the glass (about 5° drop). The main advantage of this furnace is its rapid heating time (a few

58) A. G. Worthing, Phys. Rev. 28, 190 (1926).

53
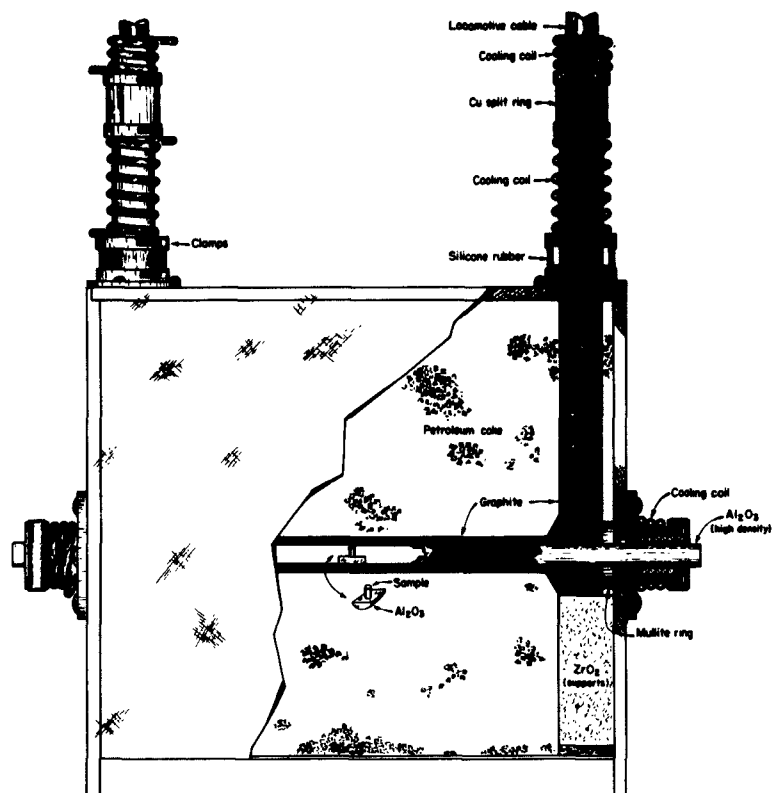
Fig. 30. Graphite resistance furnace.

minutes); its greatest disadvantage is the small zone of uniform heating, barely adequate for sintering 5-mm-diam. samples.

More uniform heating is provided in a second resistance furnace, made of graphite with larger dimensions (Fig. 30). The heater tube, 25 x 2 x 1/8 inch, has integral thick-walled end sections tapped for graphite leads. The tube is sur-rounded outside by a metal jacket filled with petroleum coke and inside by a high-density alumina tube. An argon atmosphere protects both surfaces from oxidation. The sample zone within the alumina reaches 1700°C within one hour with an input of 1100 amp at 6 volts. Later in the program the graphite heater was replaced by higher resistance carbon to achieve longer life and greater efficiency.

For hot-pressing, induction heater power is supplied by a 15-kw, 10-kc motor generator set in the general arrangment of Fig. 31. The die, used mainly for $BaTiO_3$, has the construction details shown in Fig. 32.[59] The dry-pressed pellet is placed in coarse zirconia sand between two zirconia plungers which fit in a cylindrical sleeve. The sleeve is surrounded by a steel-alloy susceptor, which

59) A. Brown, U.S. Army Signal Res. and Dev. Laboratory, Fort Monmouth, N.J., private communication.
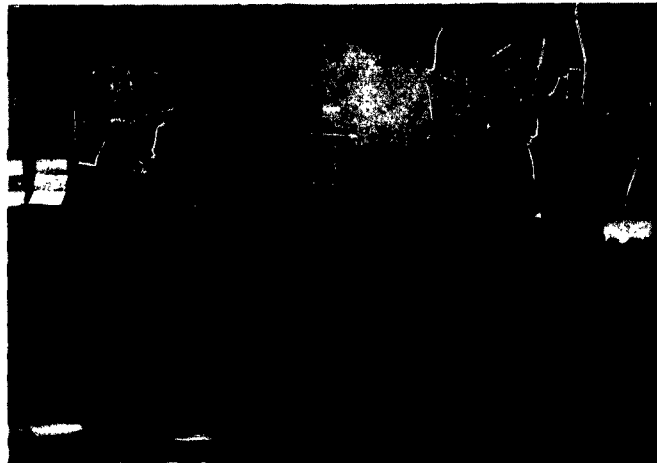
Fig. 31.

Hot-pressing unit.
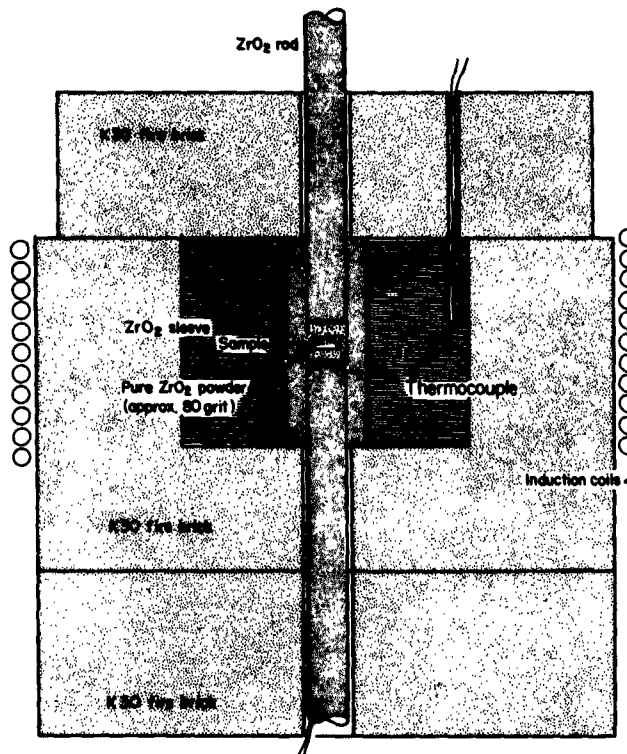
Fig. 32.

Die for hot-pressing at 1200°C.

provides mechanical support to the zirconia parts. The space between susceptor and water-cooled primary coil is filled with high-temperature bricks. This equipment is limited to 1200°C by the low melting point of the steel susceptor, and to 5,000 psi by the strength of zirconia at elevated temperatures. The temperature is measured with a thermocouple at two points, underneath the sample and within the susceptor.
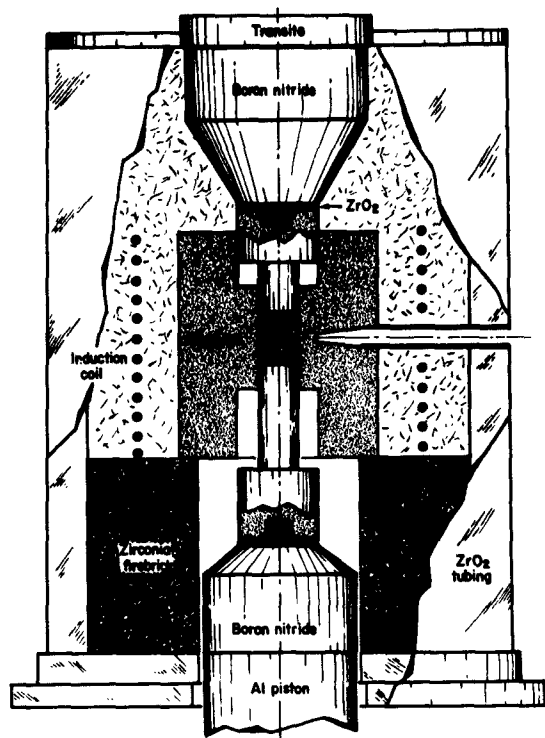
Fig. 33.

Hot-pressing unit for temper-
atures up to 2000°C.

Another die assembly, which allows working temperatures up to 2000° C.
with an average pressure of 3,000 psi is shown in Fig. 33.[60] The plunger and
susceptor are made from a high-compressive graphite compound (AGX, National
Carbon Company), which seems at present to be the only choice for this elevated
temperature. In addition, the plungers have a special shape which provides large
mechanical stability. The graphite parts are enclosed in a zirconia tube which
allows the presence of a protecting atmosphere. The temperature is measured
through a sighting tube with a pyrometer.

One of the objectives of the ferroelectric program was to study samples of
small grain size. Since these are probably best prepared by cold-pressing, we
have constructed a 425-ton press (Fig. 34) capable of squeezing the samples to
possibly 100,000 atm by use of a Bridgman-type anvil.[61] The maximum pressure
achieved up to now without cracking the dies is about 70,000 atm; with new dies[62]
we expect to reach a limit of ca. 400,000 atm.

60) B. Lersmacher et al., Arch. Eisenhüttenw. 32, 421 (1961).

61) P. W. Bridgman, J. Appl. Phys. 12, 461 (1941).

62) A. S. Balchan and H. G. Drickamer, Rev. Sci. Instr. 31, 511 (1960).
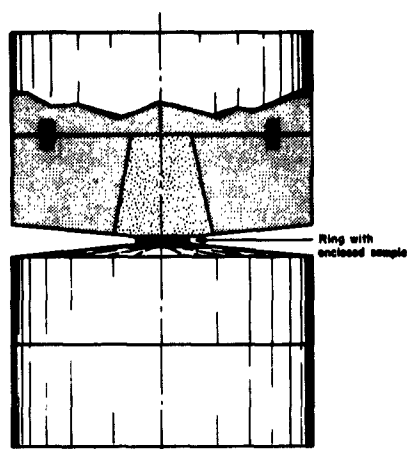
Fig. 34.

Bridgman-type dies.

Testing Methods and Equipment

Densities of samples > 95% of theoretical were determined by comparing their weights in air and in toluene. For less dense samples, connecting pores were likely to allow penetration of toluene; here a volume determination combined with dry weight in air were used.

For establishing grain sizes, we used the replica technique of electron microscopy,[63] which is faster and more effective than the usual polishing and etching. One side of a 0.1-mm thick foil of acetobutyrate (Triafol BN, Bayerwerke, Germany) was wetted with methylacetate and pressed for 30 seconds against a molded or cracked surface of a sample. After 10 to 30 minutes, depending on surface conditions, the foil was removed and placed between two microscope slides. A normal transmission microscope is sufficient for most observations, but a phase-contrast microscope is more suitable for finer details.

The only electrical properties measured were dielectric constant and loss; electric-strength measurements were not considered worth while except where densities > 99% of theoretical were achieved. Temperature runs were made mainly on a General Radio 716 CM bridge provided with automatic balancing at 200 kc. Frequency runs involved other bridges, susceptance-variation equipment, and a few resonant-cavity measurements. Unless otherwise specified, the measuring field strength was low, in the initial range 10 to 40 volts per cm.

Starting Powder

For most of our experiments the starting powder was high-purity $BaTiO_3$, Grade MP-783 (National Lead Co., Titanium Alloy Manufacturing Division). Table 7 shows the spectrographic and chemical analyses. This powder was pre-

63) R. Dallendörfer, Silikat Tech. 9, 510 (1958).

Table 7. Analysis of $BaTiO_3$ (TAM - Grade MP-783).

Spectrographic analysis

SiO_2	- 0.08%	Mn	- 0.0005%
Fe_2O_3	- 0.003%	W	- 0.01%
Al_2O_3	- 0.002%	V	- 0.002%
Sb_2O_3	- 0.002%	Cr	- 0.002%
SnO_2	- 0.001%	Nb	- 0.01%
Mg	- 0.002%	Na	- 0.01%
Cu	- 0.0001%	Ca	- 0.001%
Pb	- 0.002%	Sr	- 0.10%

Chemical analysis
BaO - 65.7%
TiO_2 - 34.3%

pared by an oxalate precipitation method resulting in an average particle size between 1 and 10 μ. A second powder was prepared in our laboratory[*] by means of chemical reaction between a titanium ester and $Ba(OH)_2$, leading to a $BaTiO_3$ precipitate in the colloidal size. This latter is supposed to be chemically pure and has an average particle size of about 0.01 μ.

Comparisons of starting and fired samples by spectrographic analysis showed no increase in impurities regardless of the forming method.

Physical Properties

The cubic-to-hexagonal phase change in $BaTiO_3$ at about 1450°C limits monophase firing to about 1400°C. The advantages of fast firing for pure materials (without grain-growth inhibitors) were clearly demonstrated by the better reproducibility and higher density obtained in the small resistance furnace (Table 8). Figure 35 shows the grain structures. Higher-temperature firing, in the hexagonal phase, resulted in densities up to 97% of theoretical (Table 9) and a grain growth as shown in Fig. 36.

Melting according to the schedule of Fig. 37 resulted in high-density (98%) hexagonal samples of good reproducibility. The 20-min. soaking time was critical, long enough to remove bubbles, short enough to prevent reduction. The

[*] Cf. pp. 50 and 51.
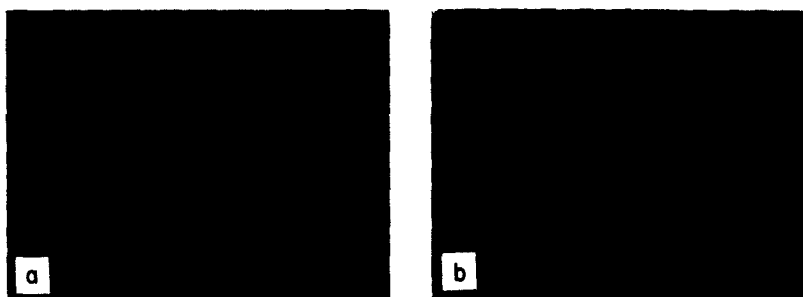
Fig. 35.   Sintered BaTiO$_3$.   (a) Globar-sintered, average   grain size 80 μ.
(b) resistance-sintered, average   grain size 50 μ.
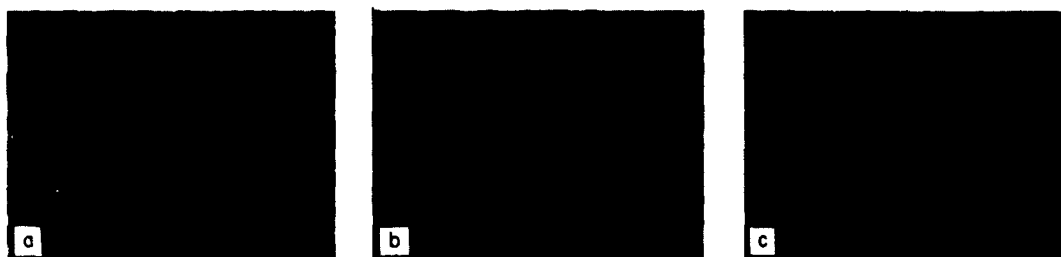
Fig. 36.   Sintered hexagonal BaTiO$_3$ (Titanium Alloy Manufacturing Division,
National Lead Co.).   (a) Resistance-sintered, average   grain size 40 μ;
(b) graphite-sintered, average   grain size 80 μ; (c) graphite-sintered,
average grain size 120 μ.
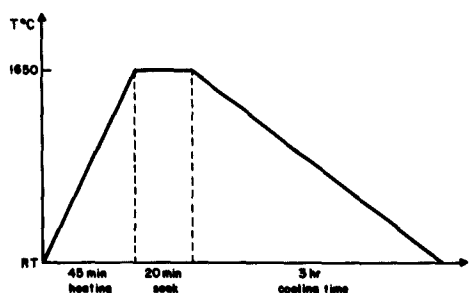
Fig. 37.

Temperature-time dependence
for hexagonal BaTiO$_3$.

schedule of Fig. 38 resulted in brittle tetragonal samples, 97 to 98% dense.   The
grain structures (Fig. 39) show sizes from 1 to 100 μ.   Nucleation apparently begins
at the walls of the container and proceeds slowly toward the interior; during re-
crystallization grains grow further.

The soak-parameter effects during hot-pressing are indicated in Table 10.

59

Table 8. Results of low-temperature sintering for Tamco $BaTiO_3$.
(Soaking at 1400°C)

Furnace	Heating time	Soak time	Cooling time	Density (%)	Grain size (μ)	Reproducibility
Globar	30 hr	12 hr	24 hr	80-85	100-200	Unsatisfactory
Globar	20 hr	10 hr	12 hr	85-90	80-120	Unsatisfactory
Resistance-strip furnace	1 min	1 hr	1 min	92	40-50	Satisfactory

Table 9. Results of high-temperature sintering for Tamco $BaTiO_3$.
(Soaking at 1600°C)

Furnace	Heating time	Soak time	Cooling time	Density (%)	Grain size (μ)
Graphite tube	80 min	20 min	3 hr	91	60
		40 min		90	100
	40 min	20 min	3 hr	93	40
		40 min		92	80
	40 min	20 min	2 hr	94	40
		40 min		93	80
Resistance-strip furnace	1 min	10 min	1 min	94	15
		20 min		97	20
		40 min		97	30
		80 min		93	50

Table 10. Limits for hot-pressing Tamco $BaTiO_3$.

Soak parameters	Low limit	Effect	Optimum condition	High limit	High-limit effect
Time	10 min	porous sample	20 min	80 min	Cracked sample
Temperature	1100°C	porous sample	1200°C	1400°C	Reduced sample
Pressure	4000 psi	porous sample	5000 psi	10.000 psi	Laminated sample
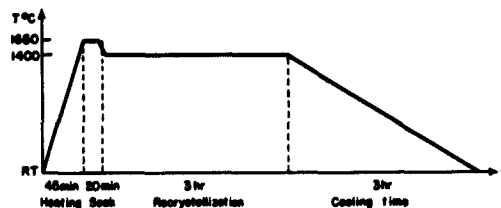
Fig. 38.

Temperature-time dependence for tetragonal BaTiO$_3$.
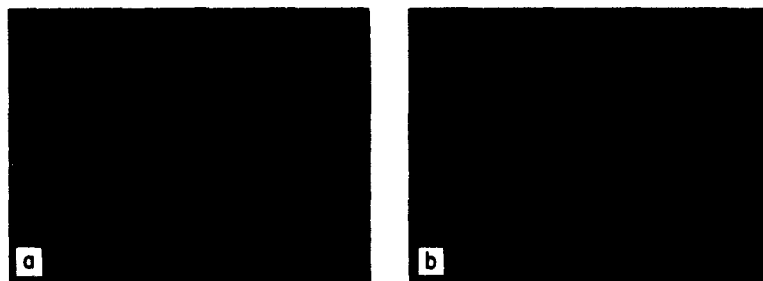
Fig. 39. Hexagonal Tamco BaTiO$_3$ from the melt. (a) Rapidly cooled, grain size 1 μ; (b) slowly cooled, grain size 100 μ.
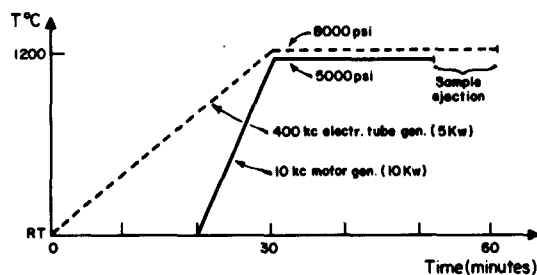
Fig. 40.

Temperature-time-pressure dependence for hot-pressing of BaTiO$_3$.

The dependence on generator input is shown in Fig. 40. At optimum conditions a density of 98% is regularly achieved. The average grain size is about 5 μ with a narrow distribution of sizes (Fig. 41). These hot-pressed samples contain much strain energy which, however, can be reduced by careful annealing. Optimum annealings, as indicated in Fig. 42, avoid irregular grain growth and voids and result in control of grain sizes (Figs. 41b, c, d, e). The density falls successively to 94% for the longest anneal.

The fine-grain laboratory powder, which hot-sintered to a density of only 85%, was hot-pressed to 95%.

The high-temperature pressing unit has not been successfully used because of chemical reduction of the sample and chemical reactions with the embedding
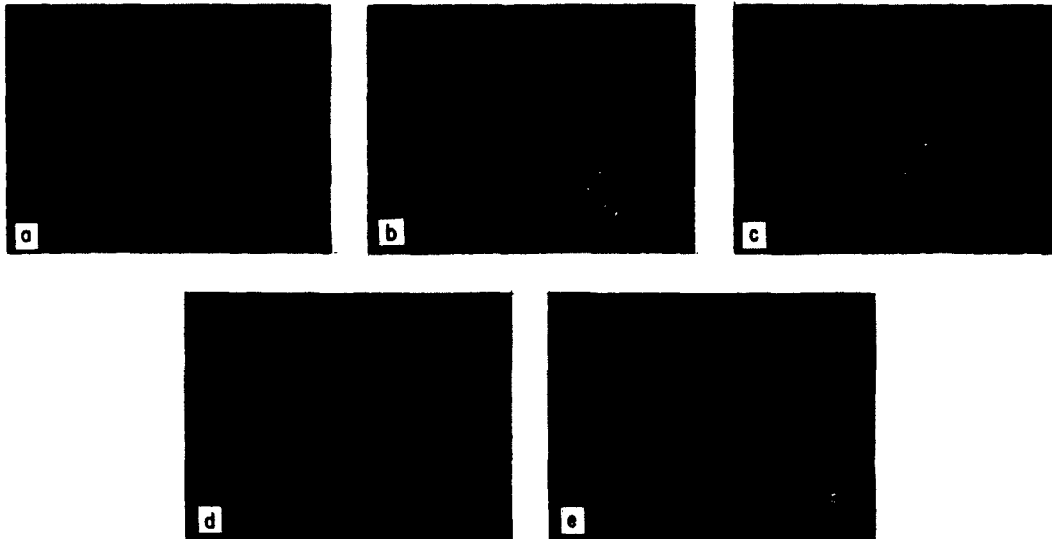
Fig. 41. Hot-pressed BaTiO₃. (a) Hot-annealed, average grain size 5 μ;
(b) annealed for 1 hour at 1270°C, grain-size ranges 10-80 μ;
(c) annealed for 2 hours at 1310°C, grain-size ranges 20-60 μ;
(d) annealed for 4 hours at 1350°C, grain-size range 20-70 μ;
(e) annealed for 8 hours at 1380°C, average grain size 100 μ.
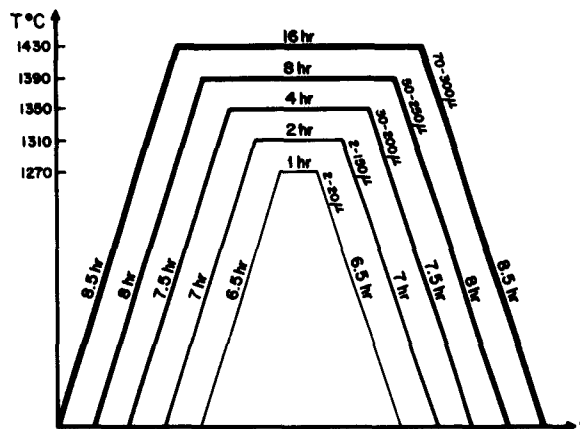
Fig. 42.

Optimum annealing conditions
for hot-pressed BaTiO₃ (with
corresponding grain sizes, in
microns).

powder.

Table 11 is a summary of optimum forming processes.

Electrical Properties

For single crystals, the dielectric constant and loss vary with temperature
(Fig. 43) when measured at low field strengths and moderate frequencies. These

Table 11. Summary of forming methods for $BaTiO_3$.

Forming method	Working temp.	Applied pressure	Phase	Density (%)	Grain size (μ)
Tamco Mp-783					
Sintering	1450	-	tet.	95	20
	1600	-	hex.	97	150
Melting	1618	-	hex.	98	1-100
Hot-annealed	1400	-	tet.	94-96	20
Hot-pressed	1200	5000 psi	tet.	98	~5
Hot-annealed	1400	-	tet.	94-96	50
Cold-pressed	30	50,000 atm	tet.	85	-
Insulation Lab.					
Hot-pressed	1200	5000 psi	tet.	95	-
Hot-annealed	1400	-	-	94	-
Cold-pressed	30	70,000 atm	tet.	60	-
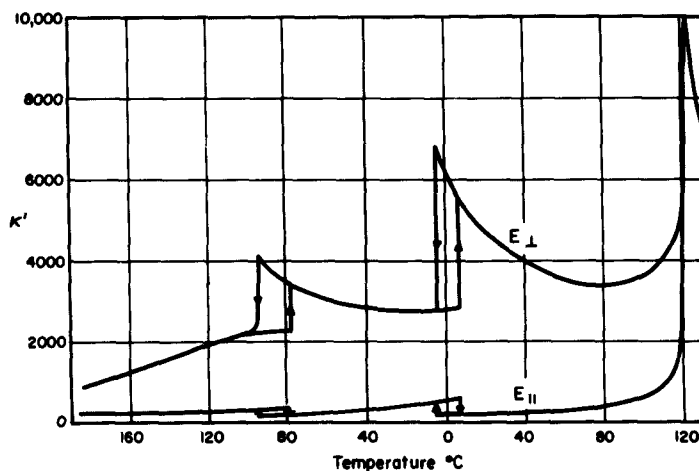
Fig. 43.

Temperature dependence of dielectric constants of $BaTiO_3$ single-domain crystal.

data can be averaged to obtain a theoretical curve for an "ideal" ceramic sample which is compared in Fig. 44 with typical characteristics for our ceramics . Because of ageing effects the data near room temperature and below are not useful for comparisons. Other features of the curves are:

1. Temperature for peak dielectric constant, T_c. This may be either raised or lowered by impurities but is always depressed by strain.

2. Peak value of the dielectric constant, K_c. Since this value depends on
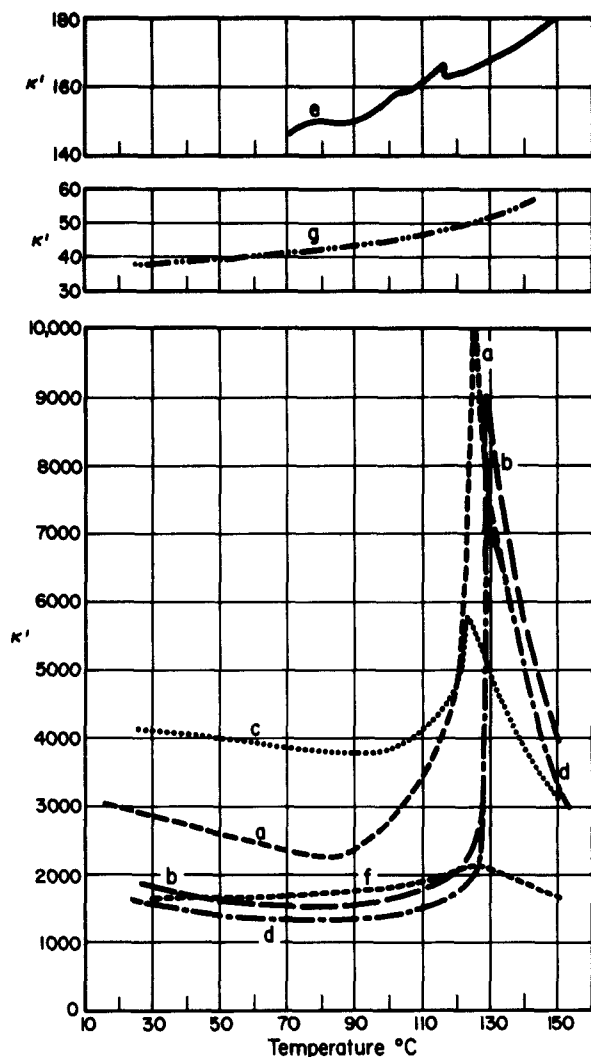
Fig. 44.

Average κ' for (a) $BaTiO_3$ crystal probably with impurities; Tamco $BaTiO_3$ (b) sintered, (c) hot-pressed, (d) hot-pressed and annealed, (e) cold-pressed; fine powder $BaTiO_3$, (f) hot-pressed at 60,000 atm, (g) cold-pressed at 69,000 atm.

all parts of the sample simultaneously changing phase and is reduced by strains and possibly by small grains, it is a very sensitive parameter.

3. Value of the dielectric constant in the minimum between phase transitions $T_{80°C}$. This involves domain-wall motion and therefore is also strain-sensitive. It is low in the presence of a large number of single-domain grains but can be high in crystallites oriented perpendicularly to the field.

Based on these features and on the data of Table 12, the hot-pressed samples are highly strained and isotropic. Fast sintering, melting, and hot-pressing followed by annealing, all produce samples with similar properties. The hot-pressing seems most easily controllable. Samples of more than 95% density

64

Table 12. Dielectric properties of Tamco BaTiO$_3$ (MP-783) at 100-200 kc with decreasing temperature at 10 volts/cm.

A. Sintered or melted samples

Firing	Sample No.	κ' 80°C	κ' peak	T°C for peak κ'
Globar	II 14.1	1350	7110	130
	II 4.3	370	8280	129.3
	II 10.1	1660	8560	130
	II 2.5	1500	7930	130.5
	Mi	1330	9050	128.8
Resistance-strip furnace	RG 1.5	850	7000	128.2
	1.6	1450	6440	129.2
	1.7	1400	5940	128.5
Melt	III 142.1	1160	5630	126.8
	III 142.2	800	6450	126.6
	II 145IR	104	173.6	127.5

B. Hot-pressed, no anneal, 2-10 μ grain size, 98% density

	Sample No.	κ' 80°C	κ' peak	T°C for peak κ'
Time of pressing:				
10 min. E ∥ press. dir.	III 97.1	3810	5730	122.5
10 min. E⊥ " "	III 97.1	4000	6110	122.5
	III 85.2	3830	5780	123
	III 85.1	3820	5812	123
	III 92.1	4110	6010	121
	III 94.1	3700	5495	120
	III 95.1	4030	6135	122

Table 12 (cont.)

C. Hot-pressed 20 min., annealed

Annealing time	Temp. °C	Grain size (μ)	Sample No.	κ' 80°C	κ' peak	T°C for peak κ'
0		2-10	III 85.2	3830	5780	123
1 hr	1270	2-20	III 88.1	3920	6040	127.2
1 "	1270	2-20	III 88.2	3390	6200	126.65
2 "	1310	2-150	III 83.1	1200	6920	129.1
2 "	1310	2-150	III 83.2	1185	6680	129.25
4 "	1350	30-200	III 87.1	1345	7005	128.6
4 "	1350	30-200	III 87.2	1325	6910	129.5
8 "	1390	20-150	III 91.1	1315	7760	129.6
8 "	1390	50-250	III 91.2	1215	7480	129.4
16 "	1430	20-150	III 90.1	1344	7275	128.75

D. Cold-pressed, 60,000 atmospheres

				150	167	116.5
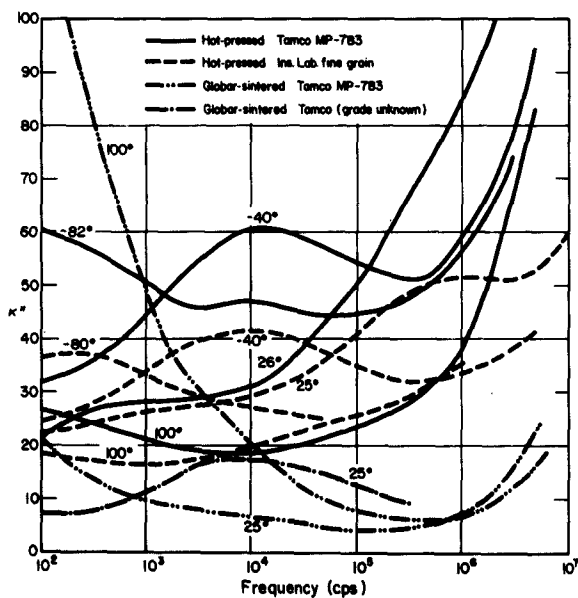
Fig. 45.

Dielectric loss factor for four different BaTiO$_3$ ceramics.

could not be made strain-free by any forming method.

Further inspection of dielectric properties in the Curie region shows that two samples seldom behave alike within limits of error of measurement ($\sim$1% for identical time temperature runs).

Frequency runs (Fig. 45) show a polar loss in all samples.

Dielectric and X-Ray Studies of $Ca_xBa_{1-x}TiO_3$ and $Ca_xSr_{1-x}TiO_3$

Ceramics of $Ca_xBa_{1-x}TiO_3$ and $Ca_xSr_{1-x}TiO_3$ have been prepared and their dielectric and structural properties investigated. Firing conditions were adjusted to obtain sharp X-ray back reflections. The Curie point of $Ca_xBa_{1-x}TiO_3$ increases with Ca concentration up to $136^\circ C$ for x = 0.08 and then decreases. Both the tetragonal-orthorhombic and the orthorhombic-rhombohedral transition points of $Ca_xBa_{1-x}TiO_3$ decrease monotonically with increasing Ca concentration (Fig. 46). $Ca_xSr_{1-x}TiO_3$ solid solutions with $0.01 \leqslant x \leqslant 0.10$ are ferroelectric at very low temperatures. $SrTiO_3$ assumes a tetragonal structure below about $80^\circ K$.
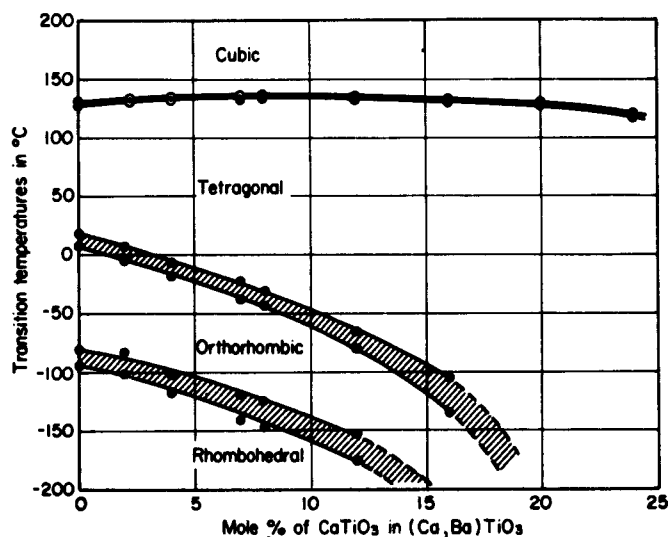
Fig. 46. Transition temperatures of $Ca_xBa_{1-x}TiO_3$ vs. molar ratio x. (Shaded areas represent temperature hysteresis.)

Dielectrics Containing Bismuth

Bismuth Perovskites

The possibilities of introducing Bi in the A sites of perovskite-type structures have been investigated. $Bi_{0.5}Na_{0.5}TiO_3$ and $Bi_{0.5}K_{0.5}TiO_3$ were found to be of this structure type and to be ferroelectric with Curie temperatures at 310° and $370^\circ C$, respectively. Solid solutions between them and between the

latter and $BaTiO_3$ also proved to be ferroelectric perovskites. Substituting Rb or Li for Na or K did not lead to perovskite structures.

A similar study concerned $PbZrO_3$, where up to 50% of the Pb ions were substituted for $(BiNa)_{0.5}$ or $(BiK)_{0.5}$, respectively. The dielectric behavior of these new compounds is very similar to that of $PbZrO_3$.

Investigation of the Bi_2O_3-TiO_2 System

Apart from the well-known ferroelectric $Bi_4Ti_3O_{11}$ a new compound, Bi_2TiO_{11}, was found (confirmed by a recent publication[64]). The unit cell was shown to be monoclinic side-centered $\left[$on (001)$\right]$ with paramaters a = 14.56 A, b = 3.80 A, c = 14.91 A, β = 93.2°, and containing 4 formula units. A phase transition at 250°C agrees with that formed by Subbarao.[64] The unit cell at 300°C is also side-centered monoclinic but contains only 2 formula units. At room temperature a small amount of a red-colored phase is present, in contrast to the yellow $Bi_2Ti_4O_{11}$. The powder pattern can be indexed on the following monoclinic cell: a = 3.70 A, b = 11.82 A, c = 9.73 A, β = 99.8°. This phase contains proportionately more impurities than the yellow phase.

Fe^{4+} in $LaFeO_3$-$SrFeO_3$ and $SrFeO_3$-$SrTiO_3$ Systems

The presence of Fe^{4+} in both the $LaFeO_3$-$SrFeO_3$ and the $SrFeO_3$-$SrTiO_3$ systems has been determined by the combined evidence of chemical and structural analysis as well as by electrical and magnetic measurements on a series of compositions. The common member of both systems, $SrFeO_3$, cannot be prepared as a stoichiometric compound when fired in an oxygen atmosphere; rather, a compound $SrFeO_{2.8}$ is formed. In the $LaFeO_3$-$SrFeO_3$ system a maximum in the conductivity, magnetization, and optical absorption occurs when the composition corresponds to $La_{0.5}Sr_{0.5}FeO_3$. This is also the point where equal numbers of Fe^{4+} and Fe^{3+} are present. Of particular interest is the thermoelectric voltage which here changes sign (Fig. 47). The room-temperature conductivity at this point is 10^2 ohm^{-1} cm^{-1}, while for $LaFeO_3$ it was only 8×10^{-5} ohm^{-1} cm^{-1}.

Some similarities of the observed characteristics of the $SrFeO_3$-$SrTiO_3$ with the $LaFeO_3$-$SrFeO_3$ system should be noted. The thermoelectric voltage in the former also passes through 0, not where Fe^{4+} and Fe^{3+} are present in equal numbers, but at a composition $SrFe_{0.8}Ti_{0.2}O_3$ which has an Fe^{4+}/Fe ratio of 70%.

The room-temperature conductivities of the two systems are not easily compared since $LaFeO_3$-$SrFeO_3$ was measured at 18 cps while the other system was measured at 10^5 cps. However, the lower value of the 10^5-cps measurement on $SrFeO_3$ is in qualitative agreement with the 10-ohm^{-1} cm^{-1} value found for 18 cps.

64) E. C. Subbarao, J. Am. Ceram. Soc. 45, 564 (1962).
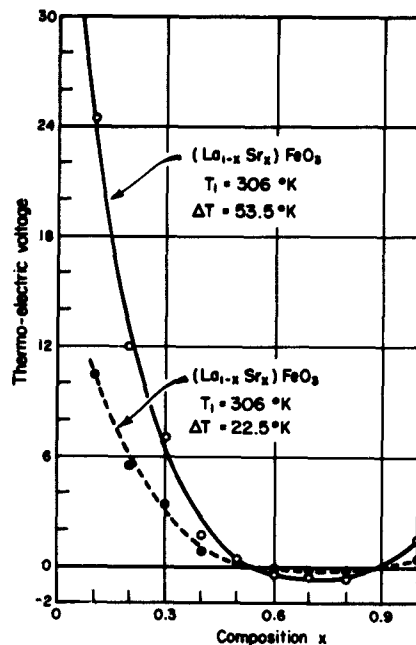
Fig. 47.

Thermoelectric voltage vs. composition of $La_{1-x}Sr_xFeO_3$.
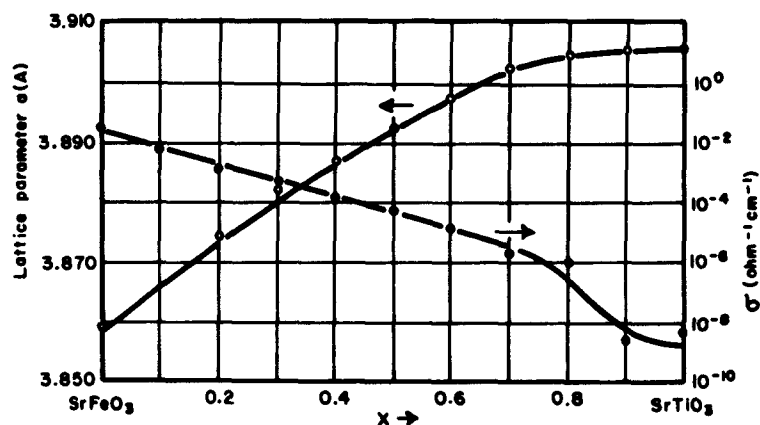
Fig. 48. Lattice parameter and room-temperature conductivity at 10^5 cps for $SrFe_{1-x}Ti_xO_3$.

In the $SrFeO_3$-$SrTiO_3$ system a marked break in the conductivity occurs at $SrFe_{0.2}Ti_{0.8}O_3$. Further increase in iron causes an increase in σ of two orders of magnitude. The break corresponds to a marked decrease in the lattice parameter and the first appearance of Fe^{4+} in the chemical analysis (Fig. 48).

Both systems exhibit antiferromagnetic behavior, with the strontium-rich
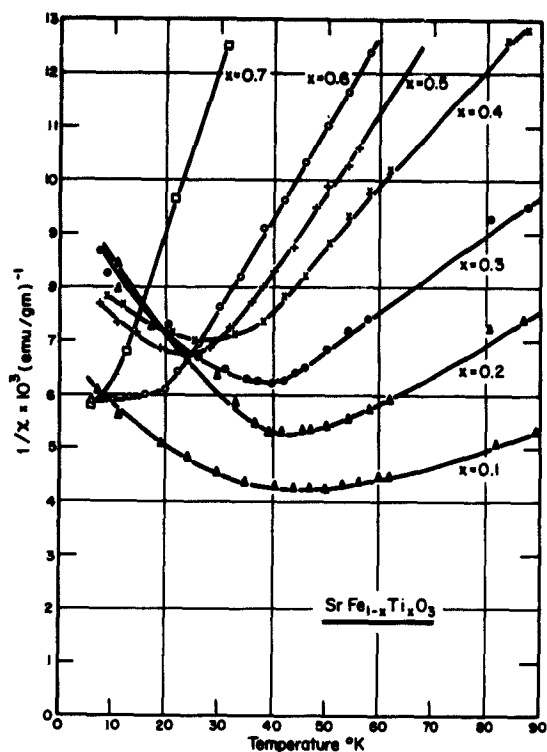
Fig. 49.

Inverse magnetic susceptibility of $SrFe_{1-x}Ti_xO_3$ vs. temperature.

compositions having Néel temperatures below $60^\circ K$ (Fig. 49) while lanthanum-rich compositions have increasingly high T_N.

The appearance of a parasitic moment in the $SrFeO_3$-$SrTiO_3$ system is associated with a preferential alignment of the Fe^{3+} in the direction of the applied field and is quite sensitive to the Fe^{4+}/Fe^{3+} ratio and the cooling field. An example of such behavior is shown in Fig. 50.
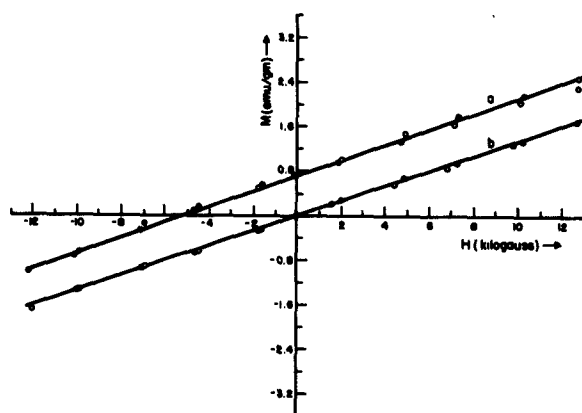
Fig. 50. Magnetization vs. field at $5^\circ K$ for $SrFe_{0.8}Ti_{0.2}O_3$ cooled in (a) 12.8-gauss and (b) zero field.

70

An Apparatus for the Determination of the Temperature Coefficients
of Dielectric Constants of Ionic Crystals

A theoretical understanding of $d\kappa'/dt$ presupposes experimental information of the thermal expansion, compressibility, and the pressure dependence of the dielectric constant. A sample holder (Fig. 51) was constructed for measurements of $d\kappa'/dt$, $d\kappa'/dp$, dl/dt, and dl/dp from 0 to 150°C at pressures up to 3000 atm. For measurements of $\Delta\kappa'$, the sample is silver-coated, except for two coupling windows, and acts as a dielectric-filled cavity. Two coupling loops allow observation of the resonant microwave frequency in transmission. A coaxial standing-wave detector measures frequency changes in the arrangement of Fig. 52. For KCl, $(1/\kappa')(d\kappa'/dp)$ at 25°C was linear to 1500 psi at 7.8×10^{-6} per kilobar.

Changes in axial length of the sample are sensed relative to iron by a co-axial-type differential capacitor connected to a capacitance bridge (Fig. 53). The balancing control in the bridge is a linear differential capacitor (Fig. 54). The sensitivity of the bridge allows balancing to 0.001 cm on the micrometer control. Since the over-all multiplying factor is 2200, a movement of 50 A is detectable at the sensing element. In measuring compressibilities, the sensor is surrounded by the pressure-transmitting fluid, hexane. The inner element is fused quartz with a higher compressibility than the iron outer electrodes; thus the sensor could be designed to compensate for the increase in κ' of the fluid with pressure (in the
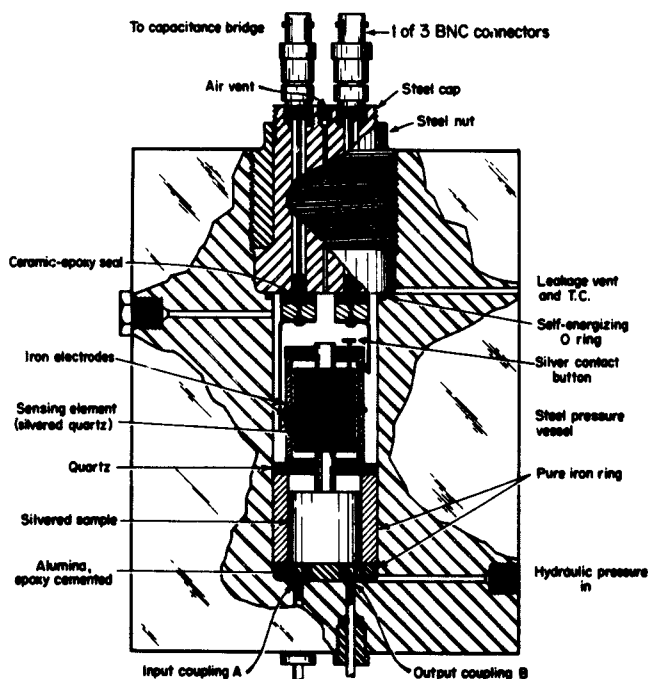
Fig. 51.

Pressure vessel for determining change in dielectric constant and axial length with pressure and temperature.
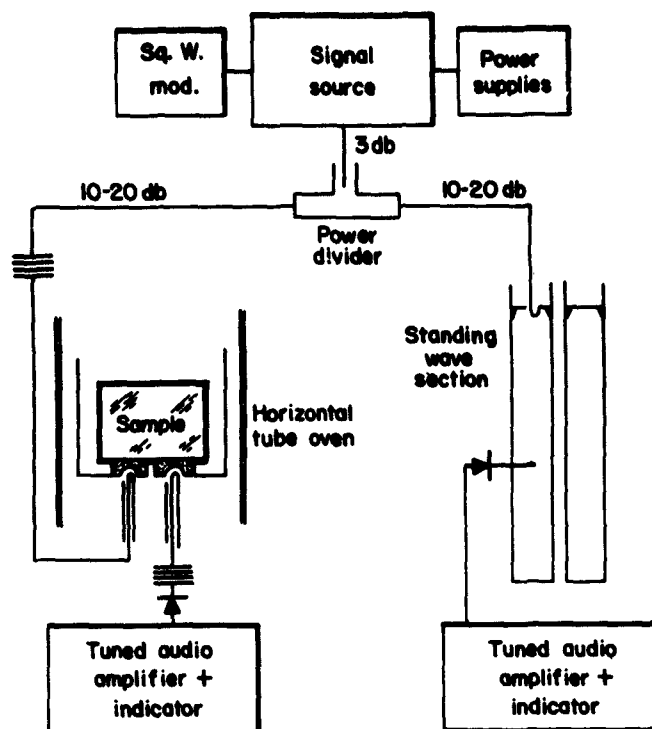
Fig. 52.

Equipment for resonant-
cavity measurements.
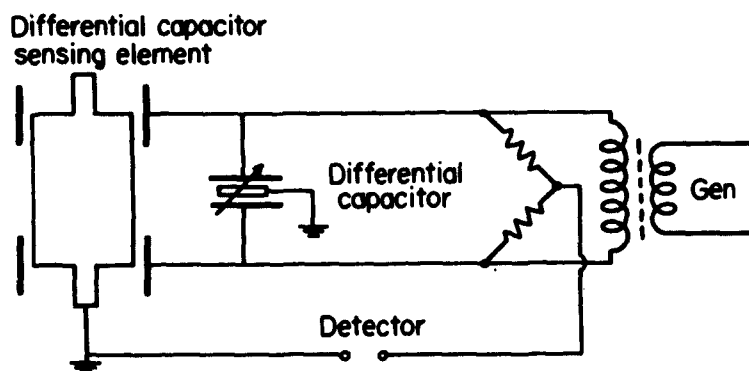
Fig. 53. Coaxial sensing unit in capacitance bridge.

linear range) with an increase in electrode spacing. The difference in compressi-
bility of copper and iron was determined to be 5.8×10^{-6} but repeated runs in-
dicated that contamination in the hexane was a serious problem. Apparently water
molecules coat the surface of the quartz and thus form a conducting surface between
the silver electrode stripes. A new magnetic sensing element (Fig. 55) has been
designed to replace the differential capacitor which will be retained for thermal-
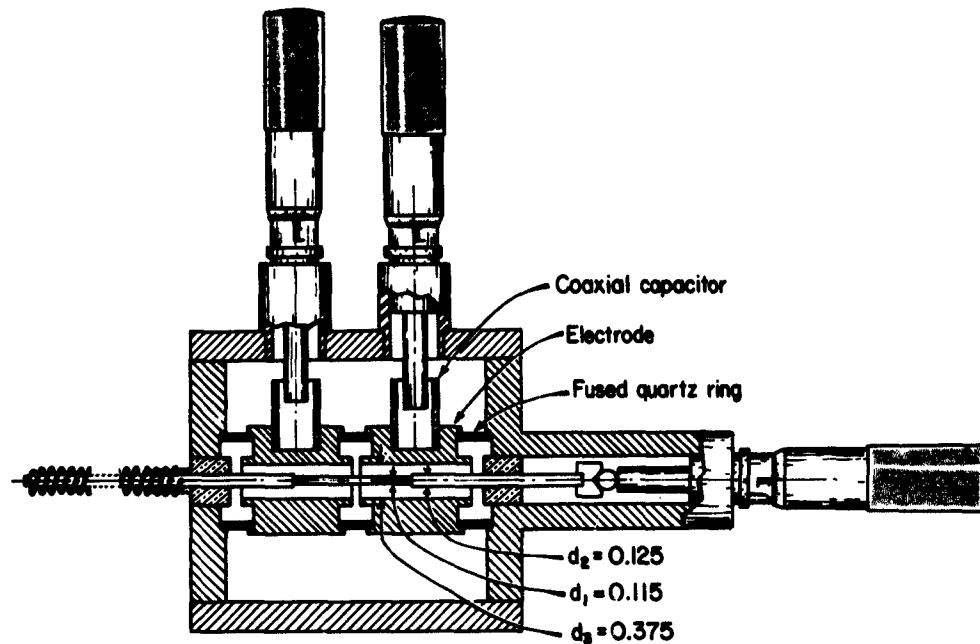
Fig. 54. Differential balancing capacitor.
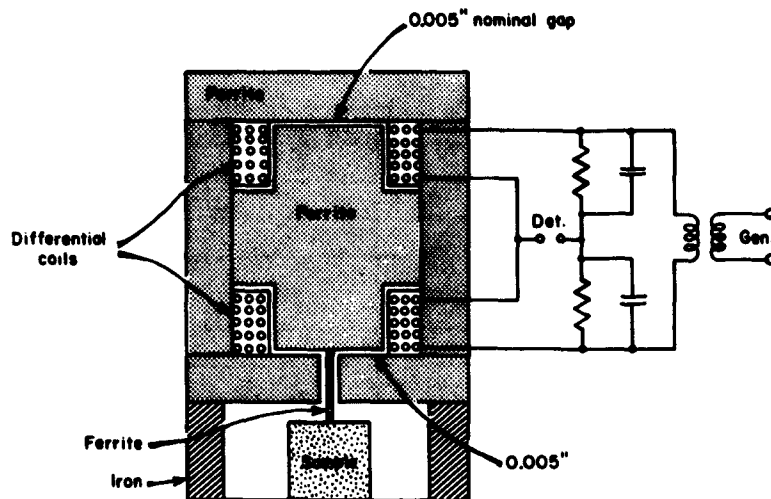
Fig. 55. Differential magnetic sensor for measurement of compressibilities.

expansion measurements.

Frequency Response of $BaTiO_3$ Single Crystals in the Microwave Region and Beyond

The dielectric constant of a barium titanate single-domain crystal has been measured as a function of temperature at 24 kMc. The method used[65] involves

---

65) Prog. Rep. No. XXXI, Lab. Ins. Res., Mass. Inst. Tech., July, 1962, p. 11.

73

measuring the standing-wave ratio in front of a thin crystal plate mounted on a quarter-wave section of quartz placed against the shorted end of a waveguide (Fig. 56). A quarter-wavelength thick quartz spacer was ground to fit the guide with a clearance of 0.0002 inch, the previously prepared $BaTiO_3$ plate being then cemented to its face with unstirred Engelhard CA9R cement. This type was selected for its transparency (allowing microscopic inspection of the mounted crystal) and for the ease with which it is cut by the air-abrasive technique used to trim the crystal edges. After insertion of the crystal-spacer sandwich in the sample holder any spaces between the crystal edges and the waveguide wall were carefully filled with silver paint.
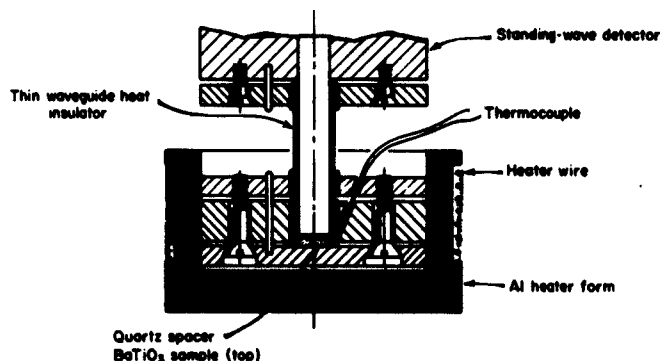
Fig. 56. Microwave sample holder.
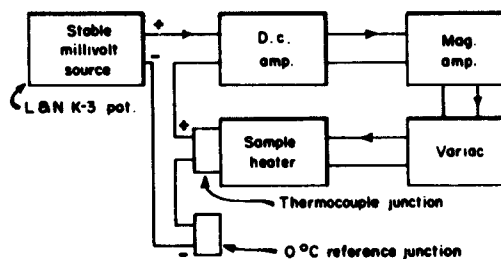
Fig. 57. Temperature-control system.

The crystal selected was etched to a thickness of 31 μ, using Last's[66] technique, and polarized into a single C domain by placing the cold crystal in an orienting electric field and then warming it through the 0°C phase transition. [67]

66) J. T. Last, Rev. Sci. Instr. 28, 720 (1957).
67) P. H. Fang, Phys. Rev. 108, 242 (1957).

74

Although a thickness of 10 μ was
desired, a plate this thin with sufficient
area to cover the cross section of a K-
band waveguide could not be obtained
from the "butterfly" crystals available.

Temperature of the mounted crys-
tal was controlled and measured to with-
in $< 0.1°C$ using the system of Fig. 57.
Results of the measurements are in-
dicated in Fig. 58. The dielectric con-
stant above the Curie point could not be
determined since in this region ϵ^* was
so high as to cause the crystal thickness
to be very close to a quarter wavelength.
This greatly decreased the measuring
precision for the distance between the

Fig. 58. Dielectric constant of $BaTiO_3$
single-domain crystal at 24 kMc.

crystal surface and the first electric field node. The values of dielectric constant
found agree with those reported earlier by Benedict and Durand.[68] The high ϵ'
values confirm that there is neither relaxation of the clamped dielectric constant
nor ionic resonance at or below 24 kMc, showing the results reported by Fousek[69]
to be in error.

The primary purpose of the present study is to investigate $BaTiO_3$ in the
spectral region in which the ferroelectric state disappears. Since the foregoing
measurements conclusively indicate that this region lies at higher than micro-
wave frequencies, emphasis will be on the millimeter-wave region, and no further
attempt will be made at microwave frequencies.

An optical system has been constructed to allow reflectivity measurements
on the millimeter-wave interferometer. It uses an angle of incidence of 10 degrees,
as close to normal incidence as the 10-degree beam spread of the spectrometer
allows; the beam cross section at the sample position has been limited to an area
10×18 mm^2. The reflection unit also provides a rotatable sample holder to
facilitate comparison of mirror and crystal reflectivities. Reflectivity measure-
ments on $BaTiO_3$ single-domain crystals are in progress, but still hampered by a
small signal-to-noise ratio, which at present does not allow unambiguous determina-
tion of results. Improvements are being made.

68) T. S. Benedict and J. L. Durand, Phys. Rev. 109, 1091 (1958).
69) J. Fousek, Czechoslov. J. Phys. 9, 172 (1959).

Protons, Dipoles, and Charge Carriers in Rutile

Experiments carried out in this Laboratory indicate the following character-istics for rutile single crystals:[70]

Pure rutile without electrodes is an insulator with an optical gap width of ca. 3 ev from the filled 2p-band of O^{2-} to the empty 3d-band of Ti^{4+}. An activa-tion energy of about 1.5 ev can transfer electrons thermally into the conduction band. At high temperature, the electron population in the 3d-band increases suf-ficiently to make it detectable by a broad absorption spectrum extending from the infrared lattice vibrations into the visible region. Any fine structure of the con-duction band is blurred out at this high temperature; at room temperature, it can be discerned for the transition into the 3d-band; it will be investigated in detail at low temperature.

The conduction in the 3d band is extremely anisotropic; the optical axis di-rection is the preferred one by several orders of magnitude, as might be expected from the crystal structure, which offers uninterrupted chains of cations in this direction. A similar preference can be expected for hole conduction by chains of anions, and our "pure" rutile crystals have in fact proved p conductors according to thermoeffect measurements up to several hundred degrees C.*

This preference of the optic-axis direction is still clearly visible in slightly reduced rutile but practically wiped out by strong reduction or high temperatures, where the conductivity reaches values $\sigma > 1 \text{ ohm}^{-1} \text{ cm}^{-1}$. The anisotropy is not caused, as Hollander and Castro[71] believe, by the reduction but is a property of the pure crystal. This becomes immediately clear by electron (and probably also hole) injection at low temperature.

Electrons (and probably holes) can be easily injected into the empty con-duction band (respectively the valence band) of rutile and can transform the insulator into a very good conductor; field-emission devices, e. g. , diodes of the Esaki type, may be realized. Diode characteristics have been observed as func-tion of time at constant voltage since the polarization and with it the field gradient at the electrodes changes as function of time. The polarization caused by the trapping of charge carriers in the volume and by blocking layers at the electrodes can be measured by dielectric relaxation spectra and by discharge characteristics, confirming the strong preference of the optic-axis direction for charge transfer in the unreduced material.

This preference is most impressively demonstrated when the injection cur-rent is raised with voltage until thermal instability by Joule heating occurs. The crystal becomes incandescent and can be maintained in that stage for days if the current is stabilized. Otherwise thermal electric breakdown results (Fig. 59)

70) A. von Hippel, J. Kalnajs, and W. B. Westphal, J. Phys. Chem. Solids 23, 779 (1962).

* Our latest measurements seem to indicate that the p-type conduction may be a freak effect.

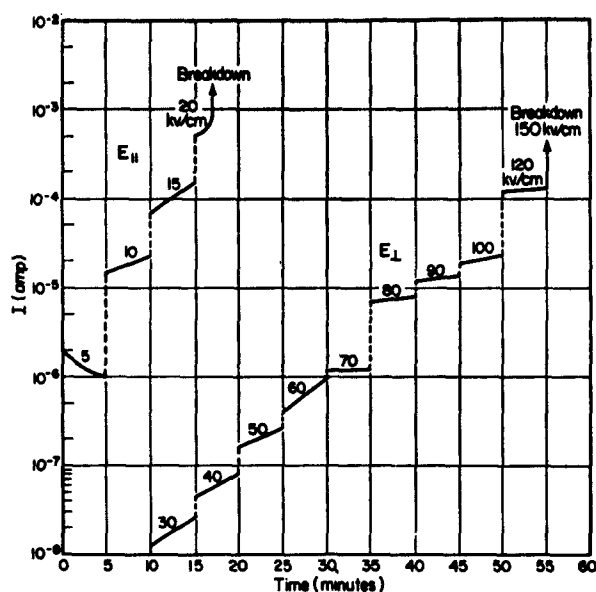71) L. E. Hollander, Jr., and P. L. Castro, Phys. Rev. 119, 1882 (1960).

Fig. 59.

D-c breakdown of rutile
single crystal parallel
and perpendicular to optic
axis (voltage raised in 5-
min. intervals).

leading to about six times smaller strength in the c than the a direction. When impulse voltage forestalls this thermal instability, the breakdown strength is more than thirty times higher and the anisotropy slightly inverted.

The rutile crystals now obtained are far from ideal. Protons are incorporated already during the growing process; their accurate position in the lattice can be identified by the detuning of the OH stretching vibration through hydrogen bonding. Reduction will initially produce anion vacancies, but a search for clear optic or electric evidence of such vacancies, by comparison of quenched with annealed samples and by paramagnetic resonance, proved unsuccessful. This failure seemed surprising in view of the 10^{20} vacancies per cm^3 predicted by the thermochemical data of Buessem and Butler, [72] but recent analytical determinations give much lower oxygen deficiencies. Furthermore, Magnéli and co-workers [73] have demonstrated the existence of at least nine oxides $Ti_{2n}O_{2n-1}$, where $n = 2 \longrightarrow 10$ and possibly $\longrightarrow \infty$, ranging all the way from TiO_2 to Ti_2O_3, a p-type semiconductor investigated in our laboratory by Pearson. [74] The existence of these oxides means that the vacancy lattice reverts into a dense structure of interstitial Ti by inserting

72) W. R. Buessem and S. R. Butler, "Kinetics of High Temperature Processes," W. D. Kingery, Ed. , The Technology Press of M. I. T. and John Wiley and Sons, New York, 1959, pp. 13 ff.

73) S. Anderson, B. Collén, U. Kuylenstierna, and A. Magnéli, Acta Chem. Scand. 11, 1641 (1957); S. Anderson, B. Collen, G. Krusse, U. Kuylenstierna, Å. Magnéli, H. Pestmalis, and S. Asbrink, ibid. 11, 1653 (1957); S. Anderson, ibid. 14, 1161 (1960).

74) A. D. Pearson, J. Phys. Chem. Solids 5, 316 (1958).

specific dislocation planes ("chemical dislocations") perpendicular to the c-axis direction. Such structure changes including the ordering of the dislocation planes may be the cause of thermal hysteresis characteristics. The insertion of more and more planes, where charge carriers are trapped and scattered as the oxygen loss increases, explains the disappearance of the anisotropic conduction on strong reduction.

The discoloration band centered near 1.5 μ seems not to be caused by electrons trapped in oxygen vacancies, as Cronemeyer[75] assumed, but by the lattice destruction accompanying the oxygen loss, allowing Ti^{4+} to trap electrons and form Ti^{3+} near oxygen vacancies or on the interstitial ions of the Magnéli interfaces. This interpretation is consistent with the paramagnetic resonance observed by Chester[76] and also with the strong surface conduction and dislocation of rutile.

Since the conductivity, and with it the permittivity, of rutile crystals depends so strongly on prehistory and experimental conditions, characteristic values must be quoted with caution. Furthermore, it is clear that data on reduced crystals (Hall effect, etc.) cannot be used with confidence for a theoretical discussion of the band structure, electron mass, and mobility of charge carriers in rutile proper as has been done in the past. Work has been started to obtain better crystals and reliable values for unreduced rutile.

CONCLUSIONS

The influence of the long-range polarization field of optical phonon modes and its mode-pulling effect, invoked by Cochran for the onset of ferroelectricity, appears greatly overrated, as our measurements on the feedback factor and other theoretical and experimental data indicate. Instead, the molecular-bond structure of the near-order array and the different temperature dependence of competing polar and nonpolar bonds may provide a satisfactory explanation for ferroelectricity and phase transitions in the perovskites. The Curie-Weiss law should then arise from a competition between the formation of phase-coherent nuclei of dipolar order, organized by short-range strain effects, and their destruction by thermal randomization.

Once the ferroelectric state becomes stabilized, the frequency response of a single-domain crystal exhibits the well-known resonance region of mechanical-distortion modes (piezoelectric resonances). In addition we should expect at much higher frequencies an electric resonance region ("dipolar acoustic" phonon modes), akin to the spin-wave resonances of ferro- and antiferromagnetics in the microwave and far-infrared regions. A search for this spectrum, which would terminate the ferroelectric response in the infrared before the normal polar modes of the

75) D. C. Cronemeyer, Phys. Rev. 87, 876 (1952).

76) P. F. Chester, Bull. Amer. Phys. Soc. 5, 72 (1960); J. Appl. Phys. 32, 866 (1961).

lattice vibrations are reached, is in progress. If this spectrum exists, it might provide a useful means for generating ultrasound waves between 10^9 and 10^{12} cps.

Extensive experiments on crystal growth by flame fusion have led to satisfactory methods for preparing feed powders for a variety of crystals and for growing these crystals under improved conditions. Still, such crystals are far from perfect and a point of diminishing returns seems to have been reached with the Verneuil technique. Substitution of the gas burner by the plasma torch may allow further advances and is under investigation.

Large, quite pure single crystals of $BaTiO_3$ have been grown by applying the pulling technique to binary melts of barium titanate with titanium dioxide. For ceramics, optimum conditions for preparing dense samples from pure powders have been established and reproducible dielectric characteristics obtained.

Studies on cation substitution in the A sites of perovskites (substituents: alkali, alkali earth, bismuth, and iron ions) led to several new ferroelectrics, allowed to force the iron ion into the Fe^{4+} state, and produced materials with interesting magnetic transitions.

Extremely high anisotropy effects were found in "pure" rutile crystals for electron transconduction and electric strength; the transfer of electrons was investigated on dielectric relaxation spectra and with infrared spectroscopy. Hydrogen can enter rutile crystals in definite amounts, be replaced by deuterium and traced to specific lattice sites, as measurements of the OH and OD stretching vibrations testified.

A new prototype model, the "distortable double well," was developed for the treatment of relaxation spectra, which indicate the "freezing-in" of carriers at low temperatures. The model can be extended to ferroelectrics.

Much additional information on preparation and characteristics of materials, on instrumentation and theoretical concepts will be found in this final report and the preceding technical reports for this project. As it should be, many new questions have been raised and work is continuing under other contracts.

ACKNOWLEDGMENT